

# A study of velocity fields in the transition region of $\epsilon$ Eri (K2 V)

S. A. Sim<sup>1,2\*</sup>, C. Jordan<sup>1</sup>

<sup>1</sup> *Department of Physics (Theoretical Physics), University of Oxford, 1 Keble Road, Oxford, OX1 3NP, UK*

<sup>2</sup> *Astrophysics Group, Imperial College London, Blackett Laboratory, Prince Consort Road, London, SW7 2BW*

2003 Jan 21

## ABSTRACT

Analyses of the widths and shifts of optically thin emission lines in the ultraviolet spectrum of the active dwarf  $\epsilon$  Eri (K2 V) are presented. The spectra were obtained using the Space Telescope Imaging Spectrograph on the *Hubble Space Telescope* and the *Far Ultraviolet Spectroscopic Explorer*. The line widths are used to find the non-thermal energy density and its variation with temperature from the chromosphere to the upper transition region. The energy fluxes that could be carried by Alfvén and acoustic waves are investigated, to test their possible roles in coronal heating. Acoustic waves do not appear to be a viable means of coronal heating. There is, in principle, ample flux in Alfvén waves, but detailed calculations of wave propagation are required before definite conclusions can be drawn about their viability. The high sensitivity and spectral resolution of the above instruments have allowed two-component Gaussian fits to be made to the profiles of the stronger transition region lines. The broad and narrow components which result share some similarities with those observed in the Sun, but in  $\epsilon$  Eri the broad component is *redshifted* relative to the narrow component and contributes more to the total line flux. The possible origins of the two components and the energy fluxes implied are discussed. On balance our results support the conclusion of Wood, Linsky & Ayres, that the narrow component is related to Alfvén waves reaching to the corona, but the origin of the broad component is not clear.

**Key words:** stars: individual ( $\epsilon$  Eridani) - stars: late-type - stars: chromospheres - stars: coroneae - line: profiles

## 1 INTRODUCTION

The observed widths (and profiles) of emission lines, formed in stellar chromospheres, transition regions and coroneae, provide valuable information on possible heating processes, in addition to that deduced from the emission line fluxes. Observations of solar line widths in the ultraviolet (uv) part of the spectrum have been carried out since 1970 (Berger, Bruner & Stevens 1970; Bruner et al. 1970) and much of the basic behaviour of these line widths was established from work in the 1970s using spectra obtained from rocket flights (Boland et al. 1973, 1975; Kjeldseth-Moe & Nicolas 1977) and from the Naval Research Laboratory’s (NRL) spectrograph on *Skylab* (Doschek et al. 1976; Feldman et al. 1976). Further work was carried out with instruments on *Orbiting Solar Observatory IV (OSO-IV)* and the *Solar Maximum Mission (SMM)*. These early observations showed that line broadening is present in excess of the thermal Doppler width

and that when interpreted in terms of a wave energy flux, this flux is essentially constant through the transition region from  $T_e \simeq 10^4$  K to  $\simeq 10^5$  K (where  $T_e$  is the electron temperature). The observed line widths were found to be very similar in the various solar locations studied. Using spectra obtained with the NRL’s High Resolution Telescope and Spectrograph (HRTS), Kjeldseth-Moe & Nicolas (1977) found that some emission lines could not be well-fitted with a single Gaussian profile, but have excess flux in a broad component. Such profiles were studied further by Dere & Mason (1993). The earliest instruments used photographic recording, which has some limitations, but the main results have been confirmed and extended using the Solar Ultraviolet Measurements of Emitted Radiation (SUMER) instrument on the *Solar and Heliospheric Observatory (SOHO)*. This has allowed line profiles to be studied with a combination of high sensitivity and high spatial and spectral resolution, at a variety of locations (see e.g. Doyle et al. 1997; Seely et al. 1997; Chae, Schühle & Lemaire 1998). Peter (2000a,b; 2001) has made systematic measurements of line widths and

\* s.sim@imperial.ac.uk

shifts in both supergranulation cell boundary and cell interior regions. We make comparisons with the results of Chae et al. (1998) and Peter (2000a,b; 2001) in later sections of this paper.

Similar studies of line widths and line shifts were made for a few late-type stars observable at high resolution with the *International Ultraviolet Explorer (IUE)* (see e.g. Ayres et al. 1983a,b; Brown et al. 1984; Jordan et al. 1987). Significant improvements over these were obtained using the Goddard High Resolution Spectrograph (GHRS) on the *Hubble Space Telescope (HST)*, and, most recently, using the greater spectral coverage and sensitivity of the Space Telescope Imaging Spectrograph (STIS). The observations with *IUE* showed the presence of line broadening in G/K-type dwarfs which is similar to that in the Sun, and broader line widths in evolved stars with hot coronae. Observations of dwarf and giant stars with the GHRS have shown the presence of excess flux in line wings, compared with single Gaussian fits to the profiles (Linsky & Wood 1994; Wood, Linsky & Ayres 1997, and references therein); the contribution of this broad component appears to increase with indicators of stellar activity.

The causes of the observed line broadening are not known, but several possible processes have been proposed. The excess width of the lines, compared with the thermal broadening, is commonly attributed to turbulence, and observed line profiles have been used to find the most-probable turbulent velocities or the root-mean-square (r.m.s.) velocities. These have been used to find non-thermal energy densities and the energy flux carried by the non-thermal motions, assuming that they are associated with the passage of waves through the atmosphere. (See e.g. Brown et al. 1984; Jordan et al. 1987; Wood et al. 1997 for stellar applications). When non-Gaussian profiles have been observed, the excess flux in the wings has been attributed to a broad component associated with ‘explosive events’ (‘microflaring’) (Linsky & Wood 1994), or, in the Sun, to the passage of Alfvén waves (Peter 2001). The effect of acoustic waves on line profiles has also been discussed (Bruner & McWhirter 1979).

The possible origins of waves in the solar atmosphere and the processes by which these and other mechanisms, in particular magnetic reconnection, may cause heating of the solar chromosphere and corona have been the topic of many papers and reviews. We have made use of reviews by Browning (1991), Narain & Ulmschneider (1990, 1996) and Zirker (1993).

Here we report observations of emission line profiles, widths and line shifts in the active dwarf  $\epsilon$  Eri (K2 V). These have been made with the STIS and with the instruments on the *Far Ultraviolet Spectroscopic Explorer (FUSE)*. The data presented here are the most complete so far published for a main-sequence star, other than the Sun.

The new observations and data reduction are described in Section 2. Analyses in terms of single Gaussian fits to the line profiles and the implications of the line widths for the energy fluxes carried by Alfvén waves and acoustic waves are discussed in Section 3. The results of the measurements of line shifts are given in Section 4. Some of the line profiles are fitted better by 2-component profiles rather than single Gaussian fits; the widths and shifts derived for the two components and their possible interpretations are described in Section 5. Our conclusions are summarized in Section 6.

## 2 OBSERVATIONS AND DATA REDUCTION

The STIS observations of  $\epsilon$  Eri have been described by Jordan et al. (2001a). The observations made with *FUSE* were obtained from the archive. In using the latter, we restrict our analyses to the lines of C II and O VI, since these were obtained with the 1a lithium-fluoride detector, which is the one used to obtain the pointing on the star. The emission lines studied and the transitions involved are listed in Table 1, together with their rest wavelengths ( $\lambda_0$ ), observed wavelengths ( $\lambda_{\text{obs}}$ ) and line widths ( $\Delta\lambda$ ), which are the full-width at half-maximum (FWHM). The rest wavelengths are taken from Kurucz and Bell (1995) or from Griesmann & Kling (2000), with the exception of that for the Fe XII line, which is based on the solar wavelength (see Jordan et al. 2001a). The observed wavelengths and comparisons with the rest values given by the above authors and by Kelly (1987) are discussed in Section 4.

The widths given in Table 1 were measured by making single-Gaussian fits to the observed spectra. Except at wavelengths above  $\simeq 1800$  Å, the background level is close to zero. At  $\lambda \geq 1800$  Å, the background was determined from the nearby continuum. Likely errors (based on the wavelength resolution of the appropriate echelle grating, the uncertainty in the background level, the goodness of the fit and comparison with fluxes found by direct integration) are given for each measurement. For some of the weakest lines the signal-to-noise ratio was judged to be too small to give reliable line widths. In addition to the Gaussian fits, for the stronger lines, interactive measurements of the width at half the peak amplitude were made. For most of the lines these agree with the Gaussian fit values, within the error bars, but for the resonance lines of C IV, N V, O VI and Si IV they are significantly smaller indicating that these profiles are not adequately described by a single Gaussian fit. These half peak-amplitude widths are also given in Table 1. It is found that the profiles of these lines are described much better by two-Gaussian fits (see Section 5).

The STIS instrumental widths are taken from the STIS WWW site, and are 1.1 – 2 pixels, depending on the wavelength and grating used. For the E140M grating, one pixel is typically  $\sim 0.015$  Å, and this instrumental broadening does not contribute significantly to the observed line widths. For the E230M grating, one pixel is typically  $\sim 0.03$  Å, which leads to significant contributions to the widths of longer wavelength lines observed with this grating (see Table 1 in Jordan et al. 2001b). The *FUSE* observations have a resolution  $R = 20,000$  (Blair & Andersson 2001), corresponding to  $\Delta\lambda \sim 0.09$  Å.

The effect of rotational broadening has been considered but is judged to be negligible. For  $\epsilon$  Eri,  $v \sin i < 2$  km s $^{-1}$  (Saar & Osten 1997) which is too small (compared to the instrumental resolution) to be detectable; it is noted however, that only a factor of a few increase in the spectral resolution would make this detectable.

## 3 NON-THERMAL VELOCITIES

Most of the permitted lines, and all of the intersystem lines, formed in the transition region are expected to be optically thin. In the transition region, line opacities can be estimated

**Table 1.** Transitions, wavelengths and widths of the emission lines studied.

Ion	Transition	$\lambda_0$ (Å)	$\lambda_{\text{obs}}$ (Å)	$\Delta\lambda_{\text{FWHM}}$ (Å)
C I	$2s^2 2p^2 \ ^3P_0 - 2s 2p^3 \ ^3D_1$	1560.310	$1560.331 \pm 0.008$	$0.135 \pm 0.008^b$
C I	$2p^2 \ ^3P_1 - 2p 3s \ ^3P_2$	1656.267	$1656.273 \pm 0.009$	$0.191 \pm 0.008^b$
C I	$2p^2 \ ^1D_2 - 2p 3s \ ^3P_1$	1993.620	$1993.642 \pm 0.016$	$0.110 \pm 0.016$
C III	$2s 2p \ ^3P_1 - 2p^2 \ ^3P_2$	1174.933	$1174.949 \pm 0.006$	$0.157 \pm 0.015$
C III	$2s 2p \ ^3P_0 - 2p^2 \ ^3P_1$	1175.263	$1175.281 \pm 0.006$	$0.155 \pm 0.015$
C III	$2s 2p \ ^3P_1 - 2p^2 \ ^3P_0$	1175.987	$1176.002 \pm 0.006$	– <sup>c</sup>
C III	$2s 2p \ ^3P_2 - 2p^2 \ ^3P_1$	1176.370	$1176.384 \pm 0.006$	– <sup>c</sup>
C IV	$2s \ ^2S_{1/2} - 2p \ ^2P_{3/2}$	1548.204	$1548.224 \pm 0.008$	$0.207 \pm 0.008$
C IV				$0.183 \pm 0.008^a$
C IV	$2s \ ^2S_{1/2} - 2p \ ^2P_{1/2}$	1550.781	$1550.788 \pm 0.008$	$0.210 \pm 0.008$
C IV				$0.177 \pm 0.008^a$
N IV	$2s^2 \ ^1S_0 - 2s 2p \ ^3P_1$	1486.496	$1486.521 \pm 0.017$	$0.210 \pm 0.050$
N V	$2s \ ^2S_{1/2} - 2p \ ^2P_{3/2}$	1238.821	$1238.828 \pm 0.007$	$0.178 \pm 0.007$
N V				$0.155 \pm 0.007^a$
N V	$2s \ ^2S_{1/2} - 2p \ ^2P_{1/2}$	1242.804	$1242.822 \pm 0.007$	$0.172 \pm 0.007$
N V				$0.149 \pm 0.007^a$
O I	$2p^4 \ ^3P_2 - 2p^3(4S)3s \ ^5S_2$	1355.598	$1355.607 \pm 0.007$	$0.065 \pm 0.007$
O I	$2p^4 \ ^3P_1 - 2p^3(4S)3s \ ^5S_2$	1358.512	$1358.523 \pm 0.007$	$0.056 \pm 0.010$
O III	$2s^2 2p^2 \ ^3P_1 - 2s 2p^3 \ ^5S_2$	1660.809	$1660.847 \pm 0.018$	– <sup>c</sup>
O III	$2s^2 2p^2 \ ^3P_2 - 2s 2p^3 \ ^5S_2$	1666.150	$1666.169 \pm 0.018$	$0.217 \pm 0.030$
O IV	$2s^2 2p \ ^2P_{1/2} - 2s 2p^2 \ ^4P_{1/2}$	1399.780	$1399.797 \pm 0.015$	– <sup>c</sup>
O IV	$2s^2 2p \ ^2P_{3/2} - 2s 2p^2 \ ^4P_{5/2}$	1401.157	$1401.186 \pm 0.008$	$0.191 \pm 0.015$
O IV	$2s^2 2p \ ^2P_{3/2} - 2s 2p^2 \ ^4P_{1/2}$	1407.382	$1407.429 \pm 0.015$	– <sup>c</sup>
O V	$2s 2p \ ^1P_1 - 2p^2 \ ^1D_2$	1371.296	$1371.327 \pm 0.007$	$0.193 \pm 0.011$
O VI	$2s \ ^2S_{1/2} - 2p^2 \ ^3P_{3/2}$	1031.912	see text	$0.194 \pm 0.015$
O VI				$0.180 \pm 0.015^a$
O VI	$2s \ ^2S_{1/2} - 2p^2 \ ^3P_{1/2}$	1037.613	see text	$0.185 \pm 0.015$
O VI				$0.165 \pm 0.015^a$
Al II	$3s^2 \ ^1S_0 - 3s 3p \ ^1P_1$	1670.789	$1670.802 \pm 0.009$	$0.213 \pm 0.018^{b?}$
Si II	$3s^2 3p \ ^2P_{3/2} - 3s 3p^2 \ ^2P_{3/2}$	1194.500	$1194.499 \pm 0.013$	$0.188 \pm 0.040^b$
Si II	$3s^2 3p \ ^2P_{3/2} - 3s 3p^2 \ ^2P_{1/2}$	1197.394	$1197.389 \pm 0.013$	– <sup>c</sup>
Si II	$3p \ ^2P_{3/2} - 3d \ ^2D_{5/2}$	1264.738	$1264.747 \pm 0.007$	$0.184 \pm 0.007^b$
Si II	$3p \ ^2P_{3/2} - 3d \ ^2D_{3/2}$	1265.002	$1265.012 \pm 0.007$	$0.157 \pm 0.007^b$
Si II	$3p \ ^2P_{1/2} - 4s \ ^2S_{1/2}$	1526.707	$1526.717 \pm 0.008$	$0.173 \pm 0.008^b$
Si II	$3p \ ^2P_{3/2} - 4s \ ^2S_{1/2}$	1533.431	$1533.435 \pm 0.008$	$0.181 \pm 0.008^b$
Si II	$3s^2 3p \ ^2P_{1/2} - 3s 3p^2 \ ^2D_{3/2}$	1808.013	$1808.069 \pm 0.015$	$0.136 \pm 0.015^{b?}$
Si II	$3s^2 3p \ ^2P_{3/2} - 3s 3p^2 \ ^2D_{5/2}$	1816.928	$1816.970 \pm 0.015$	$0.142 \pm 0.015^{b?}$
Si II	$3s^2 3p \ ^2P_{3/2} - 3s 3p^2 \ ^2D_{3/2}$	1817.451	$1817.491 \pm 0.015$	$0.117 \pm 0.015^{b?}$
Si II	$3s^2 3p \ ^2P_{1/2} - 3s 3p^2 \ ^4P_{1/2}$	2335.123	$2335.109 \pm 0.019$	$0.129 \pm 0.019$
Si II	$3s^2 3p \ ^2P_{3/2} - 3s 3p^2 \ ^4P_{1/2}$	2350.891	$2350.896 \pm 0.019$	$0.124 \pm 0.019$
Si III	$3s 3p \ ^3P_1 - 3p^2 \ ^3P_2$	1294.545	$1294.578 \pm 0.014$	– <sup>c</sup>
Si III	$3s 3p \ ^3P_0 - 3p^2 \ ^3P_1$	1296.726	$1296.758 \pm 0.014$	– <sup>c</sup>
Si III	$3s 3p \ ^3P_1 - 3p^2 \ ^3P_0$	1301.149	$1301.168 \pm 0.028$	– <sup>c</sup>
Si III	$3s 3p \ ^3P_2 - 3p^2 \ ^3P_1$	1303.323	$1303.349 \pm 0.014$	– <sup>c</sup>
Si III	$3s^2 \ ^1S_0 - 3s 3p \ ^3P_1$	1892.030	$1892.106 \pm 0.015$	$0.194 \pm 0.015$
Si IV	$3s \ ^2S_{1/2} - 3p \ ^2P_{3/2}$	1393.760	$1393.781 \pm 0.008$	$0.176 \pm 0.008$
Si IV				$0.143 \pm 0.008^a$
Si IV	$3s \ ^2S_{1/2} - 3p \ ^2P_{1/2}$	1402.773	$1402.795 \pm 0.008$	$0.175 \pm 0.008$
Si IV				$0.155 \pm 0.008^a$
S I	$3p^4 \ ^3P_2 - 3p^3(4S)4s \ ^5S_2$	1900.287	$1900.322 \pm 0.016$	$0.104 \pm 0.016$
S I	$3p^4 \ ^3P_1 - 3p^3(4S)4s \ ^5S_2$	1914.697	$1914.757 \pm 0.016$	$0.106 \pm 0.016$
S II	$3s^2 3p^3 \ ^4S_{3/2} - 3s 3p^4 \ ^4P_{3/2}$	1253.811	$1253.820 \pm 0.015$	$0.108 \pm 0.015$
S II	$3s^2 3p^3 \ ^4S_{3/2} - 3s 3p^4 \ ^4P_{5/2}$	1259.519	$1259.533 \pm 0.015$	$0.122 \pm 0.015$
Cl I	$3p^5 \ ^2P_{1/2} - 3p^4(3P)4s \ ^2P_{1/2}$	1351.656	$1351.664 \pm 0.007$	$0.061 \pm 0.007$
Fe II	$3d^6(a^5D)4s \ a^6D_{9/2} - 3d^5(a^6S)4s4p(^3P) \ z^8P_{9/2}$	1888.010	$1888.032 \pm 0.015$	– <sup>c</sup>
Fe II	$3d^6(a^5D)4s \ a^6D_{9/2} - 3d^5(a^6S)4s4p(^3P) \ z^8P_{7/2}$	1901.773	$1901.799 \pm 0.016$	$0.130 \pm 0.016$
Fe II	$3d^6(a^5D)4s \ a^6D_{7/2} - 3d^5(a^6S)4s4p(^3P) \ z^8P_{7/2}$	1915.792	$1915.817 \pm 0.016$	– <sup>c</sup>
Fe II	$3d^6(a^5D)4s \ a^6D_{7/2} - 3d^5(a^6S)4s4p(^3P) \ z^8P_{5/2}$	1926.240	$1926.278 \pm 0.016$	$0.127 \pm 0.016$
Fe II	$3d^6(a^5D)4s \ a^6D_{5/2} - 3d^5(a^6S)4s4p(^3P) \ z^8P_{5/2}$	1936.794	$1936.810 \pm 0.016$	$0.124 \pm 0.016$
Fe II	$3d^6(a^5D)4s \ a^6D_{3/2} - 3d^5(a^6S)4s4p(^3P) \ z^8P_{5/2}$	1944.134	$1944.156 \pm 0.016$	– <sup>c</sup>
Fe XII	$3p^3 \ ^4S_{3/2} - 3p^3 \ ^2P_{3/2}$	1242.00	$1241.992 \pm 0.007$	$0.21 \pm 0.04$

<sup>a</sup> Width at half the peak amplitude. <sup>b</sup> Optically thick line. <sup>c</sup> Line too weak to determine the width.

from the observed line fluxes and the mean electron pressure determined by Jordan et al. (2001b). Intersystem lines formed in the chromosphere are also estimated to be optically thin. It is harder to estimate the opacities of permitted chromospheric lines and, as will be discussed later, some of these are likely to be optically thick, and will have contributions to their line widths from photon scattering. Lines to the ground level of atoms and first ions may also be affected by interstellar absorption. The ratios of lines within multiplets and the presence of self-reversals have also been used to judge whether or not lines are optically thin.

As discussed in Section 1, the widths of optically thin emission lines in stellar uv spectra are significantly greater than the thermal Doppler width corresponding to the temperature of line formation ( $T_{\text{form}}$ ). When corrected for instrumental broadening it is usually assumed that the observed width is the result of thermal and non-thermal motions, the latter being referred to as turbulence. Since most optically thin line profiles are well described by one (or more) Gaussian components, it is assumed that the turbulent velocities follow a Maxwellian distribution (and hence produce a Gaussian line profile), and the distribution is characterised by its most probable velocity  $\xi$ . This non-thermal contribution to the line width is usually the dominant contribution to chromospheric and transition region line widths.

The total line width may be expressed as

$$\left(\frac{\Delta\lambda}{\lambda_0}\right)_{\text{obs}}^2 = \left(\frac{\Delta\lambda}{\lambda_0}\right)_{\text{therm}}^2 + \left(\frac{\Delta\lambda}{\lambda_0}\right)_{\text{inst}}^2 + \left(\frac{\Delta\lambda}{\lambda_0}\right)_{\text{non-therm}}^2 \quad (1)$$

where the subscript ‘‘obs’’, ‘‘therm’’, ‘‘inst’’ and ‘‘non-therm’’ refer to the observed total width and the contributions from thermal, instrumental and non-thermal broadening respectively. By expressing the thermal width in terms of the temperature of line formation and the non-thermal width in terms of a most probable velocity  $\xi$ , equation (1) may be written as

$$\frac{\xi^2}{c^2} = \frac{1}{4 \ln 2} \left[ \left(\frac{\Delta\lambda}{\lambda_0}\right)_{\text{obs}}^2 - \left(\frac{\Delta\lambda}{\lambda_0}\right)_{\text{inst}}^2 \right] - \frac{2k_{\text{B}}T_{\text{form}}}{m_{\text{H}}m_{\text{ion}}c^2} \quad (2)$$

giving

$$\frac{\xi^2}{c^2} = 0.361 \left[ \left(\frac{\Delta\lambda}{\lambda_0}\right)_{\text{obs}}^2 - \left(\frac{\Delta\lambda}{\lambda_0}\right)_{\text{inst}}^2 \right] - 1.84 \times 10^{-13} \frac{T_{\text{form}}}{m_{\text{ion}}} \quad (3)$$

where  $T_{\text{form}}$  is in Kelvin,  $m_{\text{H}}$  is the mass of hydrogen and  $m_{\text{ion}}$  is the mass of the emitting ion, relative to that of hydrogen.

For the chromospheric lines, formed at low temperatures, the value of  $\xi$  is relatively insensitive to the adopted value of  $T_{\text{form}}$ , but because these lines are formed over a wide range of temperatures, the actual values of  $T_{\text{form}}$  are less meaningful. For the transition region lines the value of  $\xi$  is sensitive to  $T_{\text{form}}$ , which should be regarded as only an average value. The adopted values of  $T_{\text{form}}$  are given in Table 2. For the transition region lines formed above  $\log T_e > 4.3$ , the values of  $T_{\text{form}}$  are based on the line contribution functions and the observed emission measure distribution (Jordan, Sim & McMurry 2001c; Sim 2002). New calculations of the relative ion populations by Sim (2002) have been used, which take into account the density sensitivity of di-electronic recombination. This reduces the temperature of optimum line formation compared with the zero density calculations of Arnaud & Rothenflug (1985). Overall, the values of  $T_{\text{form}}$  are

**Table 2.** Values of  $T_{\text{form}}$  adopted.

Ion	$\lambda_0$ (Å)	$\log T_{\text{form}}$ (K)
C I	1993.62	3.7
C III	1170 mult.	4.7
C IV	1550 mult.	4.9
N IV	1486.50	5.0
N V	1240 mult.	5.2
O I	1356 mult.	3.8
O III	1666.15	4.9
O IV	1401.16	5.2
O V	1371.30	5.4
O VI	1034 mult.	5.45
Al II	1670.79	4.2
Si II	1815 mult.	3.85
Si II	2340 mult.	3.65
Si III	1892.03	4.45
Si IV	1400 mult.	4.8
S I	1907 mult.	3.7
S II	1255 mult.	4.2
Cl I	1351.66	3.7
Fe II	1915 mult.	3.85
Fe XII	1242.00	6.15

expected to be accurate to within about  $\pm 0.1$  dex. Values for the chromospheric lines of O I, C I and Si II are based on Sim’s (2002) calculations with the MULTI (Carlsson 1986, Scharmer & Carlsson 1985) radiative transfer code; those for Cl I, Al II and Fe II are only rough estimates; the value adopted for Fe XII is that used by Jordan et al. (2001a).

The values of  $\xi$  found using equation (3) are given in Table 3. The errors on  $\xi$  include both the measurement errors from Table 1 and an uncertainty in  $\log T_{\text{form}}$  of  $\pm 0.1$  dex. The value in parenthesis after the total error is the contribution from the uncertainty in  $\log T_{\text{form}}$  alone. The observed line positions have been converted to velocity shifts using the rest wavelengths  $\lambda_0$  given in Table 1.

The values of  $\xi$  given in Table 3 are plotted against  $T_{\text{form}}$  in Fig. 1, including only those lines which are estimated to be optically thin. Qualitatively, this plot is similar to those found for the Sun (see e.g. Jordan 1991; Chae et al. 1998);  $\xi$  is smallest in the chromosphere, rises in the low transition region and then flattens off. Comparing optically thin lines in common with those of Chae et al. (1998), the range of  $\xi$  is slightly smaller in  $\epsilon$  Eri, the widths of the mid-transition region lines are *smaller* in  $\epsilon$  Eri, but the widths of the neutral lines are on average *larger* in  $\epsilon$  Eri. All the lowest temperature chromospheric lines (those of the neutrals) are consistent with  $\xi \approx 7.5$  km s $^{-1}$ . The widths of the lowest temperature lines of Si II (the intersystem multiplet around 2340 Å) agree with this mean value. *All* the lines with  $\log T_{\text{form}} > 4.5$  have widths that are consistent with a *constant* value of  $\xi \approx 21.3$  km s $^{-1}$  throughout the mid-transition region. The other lines indicate a smooth transition between the two regimes.

There are some differences in the value of  $\xi$  for lines formed at similar temperatures, which may be due to opacity effects. The value of  $\xi$  for the Al II resonance line is larger than those for the S II lines. It is difficult to judge whether or not the observed Al II profile is self-reversed, or contains interstellar absorption, but the opacity estimate suggests that small optical depth effects could occur. The lines in the Si II

**Table 3.** Derived line shifts ( $v$ ) and turbulent velocities ( $\xi$ ). The error estimates for  $\xi$  include the total uncertainty due to the measurement errors and an assumed uncertainty in  $\log T_{\text{form}}$  of  $\pm 0.1$  dex. The errors in parentheses indicate the uncertainty due to  $\Delta \log T_{\text{form}}$  alone.

Ion	$\lambda_0$ (Å)	$v$ (km s $^{-1}$ )	$\xi$ (km s $^{-1}$ )	Ion	$\lambda_0$ (Å)	$v$ (km s $^{-1}$ )	$\xi$ (km s $^{-1}$ )
C I	1560.310	$+4.0 \pm 1.5$	–	Si II	1526.707	$+2.0 \pm 1.6$	–
C I	1656.267	$+1.1 \pm 1.6$	–	Si II	1533.431	$+0.8 \pm 1.6$	–
C I	1993.620	$+3.3 \pm 2.4$	$7.55^{+1.90(0.10)}_{-2.20(0.12)}$	Si II	1808.013	$+9.3 \pm 2.5$	$12.01^{+1.70(0.04)}_{-1.77(0.05)}$
C III	1174.933	$+4.1 \pm 1.5$	$19.50^{+2.94(0.45)}_{-3.29(0.59)}$	Si II	1816.928	$+6.9 \pm 2.5$	$12.62^{+1.67(0.03)}_{-1.74(0.04)}$
C III	1175.263	$+4.6 \pm 1.5$	$22.11^{+2.74(0.32)}_{-2.96(0.41)}$	Si II	1817.451	$+6.6 \pm 2.5$	$9.78^{+1.76(0.04)}_{-1.89(0.06)}$
C III	1175.987	$+3.8 \pm 1.5$	–	Si II	2335.123	$-1.8 \pm 2.4$	$8.07^{+1.78(0.03)}_{-1.96(0.04)}$
C III	1176.370	$+3.6 \pm 1.5$	–	Si II	2350.891	$+0.6 \pm 2.4$	$7.53^{+1.80(0.04)}_{-2.01(0.05)}$
C IV	1548.204	$+3.9 \pm 1.6$	$21.57^{+1.53(0.52)}_{-1.75(0.67)}$	Si III	1294.545	$+7.6 \pm 3.2$	–
C IV	1550.781	$+1.4 \pm 1.5$	$21.91^{+1.52(0.51)}_{-1.73(0.66)}$	Si III	1296.726	$+7.4 \pm 3.2$	–
N IV	1486.496	$+5.0 \pm 3.4$	$22.89^{+7.00(0.52)}_{-8.01(0.68)}$	Si III	1301.149	$+4.4 \pm 6.5$	–
N V	1238.821	$+1.7 \pm 1.7$	$21.82^{+2.02(0.86)}_{-2.43(1.13)}$	Si III	1303.323	$+6.0 \pm 3.2$	–
N V	1242.804	$+4.3 \pm 1.7$	$20.68^{+2.08(0.91)}_{-2.52(1.21)}$	Si III	1892.030	$+12. \pm 2.4$	$17.04^{+1.63(0.10)}_{-1.70(0.13)}$
O I	1355.598	$+2.0 \pm 1.5$	$7.79^{+1.10(0.09)}_{-1.17(0.11)}$	Si IV	1393.760	$+4.5 \pm 1.7$	$21.78^{+1.25(0.18)}_{-1.32(0.22)}$
O I	1358.512	$+2.4 \pm 1.5$	$6.42^{+1.58(0.10)}_{-1.77(0.13)}$	Si IV	1402.773	$+4.7 \pm 1.7$	$21.49^{+1.24(0.18)}_{-1.32(0.23)}$
O III	1660.809	$+6.9 \pm 3.3$	–	S I	1900.287	$+5.5 \pm 2.5$	$7.73^{+1.89(0.03)}_{-2.12(0.04)}$
O III	1666.150	$+3.4 \pm 3.3$	$21.55^{+3.83(0.39)}_{-4.19(0.50)}$	S I	1914.697	$+9.4 \pm 2.5$	$7.91^{+1.86(0.03)}_{-2.07(0.04)}$
O IV	1399.780	$+3.6 \pm 3.2$	–	S II	1253.811	$+2.2 \pm 3.6$	$15.01^{+2.27(0.06)}_{-2.33(0.07)}$
O IV	1401.157	$+6.2 \pm 1.7$	$20.82^{+2.96(0.79)}_{-3.50(1.04)}$	S II	1259.519	$+3.3 \pm 3.6$	$17.01^{+2.24(0.05)}_{-2.28(0.06)}$
O IV	1407.382	$+10. \pm 3.2$	–	Cl I	1351.656	$+1.8 \pm 1.6$	$7.50^{+1.03(0.03)}_{-1.07(0.04)}$
O V	1371.296	$+6.8 \pm 1.5$	$19.44^{+3.07(1.33)}_{-3.97(1.81)}$	Fe II	1888.010	$+3.5 \pm 2.4$	–
O VI	1031.912	see text	$24.27^{+4.60(1.20)}_{-5.75(1.61)}$	Fe II	1901.773	$+4.1 \pm 2.5$	$10.71^{+1.73(0.02)}_{-1.81(0.03)}$
O VI	1037.613	see text	$22.03^{+4.83(1.32)}_{-6.30(1.78)}$	Fe II	1915.792	$+3.9 \pm 2.5$	–
Al II	1670.789	$+2.3 \pm 1.6$	$22.67^{+2.01(0.04)}_{-2.03(0.06)}$	Fe II	1926.240	$+5.9 \pm 2.5$	$10.21^{+1.73(0.02)}_{-1.82(0.03)}$
Si II	1194.500	$-0.3 \pm 3.3$	–	Fe II	1936.794	$+2.5 \pm 2.5$	$9.81^{+1.73(0.02)}_{-1.84(0.03)}$
Si II	1197.394	$-1.3 \pm 3.3$	–	Fe II	1944.134	$+3.4 \pm 2.5$	–
Si II	1264.738	$+2.1 \pm 1.7$	–	Fe XII	1242.00	$-1.9 \pm 1.7^a$	$22.46^{+8.81(1.83)}_{-13.71(2.55)}$
Si II	1265.002	$+2.4 \pm 1.7$	–				

<sup>a</sup>  $\lambda_0$  is a solar value.

multiplet around 1815 Å do not have ratios which agree with their optically thin values, and the two lines with the largest oscillator strengths (1808.01 Å and 1816.93 Å) are slightly broader than the line at 1817.45 Å and the intersystem lines of Fe II. Although these Si II lines are not self-reversed, small opacity effects could be occurring. For these reasons these lines of Si II and Al II are not used in subsequent analyses using non-thermal widths. Lines from the other multiplets of Si II have significantly larger oscillator strengths than those in the 1815-Å multiplet, and should therefore show opacity effects. The lines at 1533.43 Å and 1526.71 Å have a flux ratio which is  $\simeq 1$ , instead of the optically thin value of 2. The multiplets at shorter wavelengths have larger or similar oscillator strengths (as given in CHIANTI, Landi et al. 1999), and are therefore also expected to be optically thick. The widths of these other lines of Si II are included in Table 1, but are not included in Fig. 1.

### 3.1 Kinetic energy density

The interpretation of the line broadening in spatially integrated stellar spectra is subject to some uncertainties. Solar observations can be used to investigate the behaviour of line widths at different positions on the Sun. In both early studies (see references in Section 1) and in more recent work with SUMER (see e.g. Peter 1999), when single Gaussian fits are made to the line profiles there is little systematic difference between the widths at different solar locations and distances from the limb. In this respect, using spatially averaged spectra should give a good estimate of the typical line widths. These solar observations also show that there are no preferred directions of the motions contributing to the widths. However, in the Sun, there are line (Doppler) shifts, with (on average) red-shifts being observed in the supergranulation network regions and smaller red-shifts being observed in cell interior regions (Peter, 2000a,b). (Blue-shifts are also observed at individual locations- see Section 4.) Integrated over a star, the combined effects of these motions will contribute to the observed line widths. Peter (2000a,b)

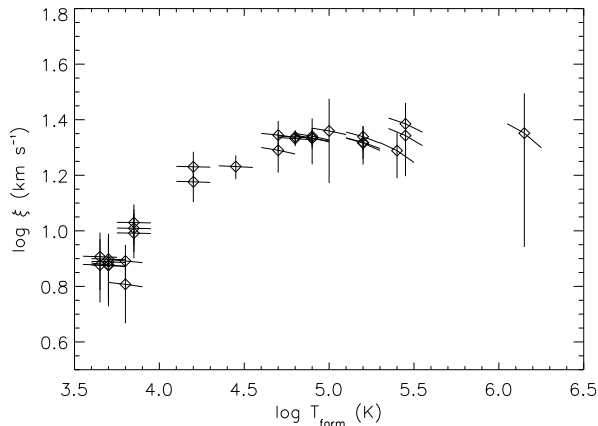


**Figure 1.**  $\log \xi$  versus  $\log T_{\text{form}}$ . The vertical error bars indicate the total uncertainty in the deduced values of  $\xi$  (including measurement errors and uncertainty in  $T_{\text{form}}$ ) and the sloping bars indicate the effects of uncertainties in  $T_{\text{form}}$ .

has made quantitative estimates of this effect by studying widths and shifts from relatively small regions with those in the mean spectrum observed over a much larger area. Using Peter's (2000b) corrected widths, the values of  $\xi$  deduced from the mean spectra would overestimate the median values by about 9 per cent (narrow component) to 15 per cent (broad components). (Two-component fits to our spectra are discussed in Section 5). For all except the stronger (alkali-like) lines, these potential contributions are less than our estimated uncertainties in the line widths.

Assuming that the line widths are due to non-thermal motions they can be used to estimate the total non-thermal kinetic energy density in the gas,  $U_{\text{NT}}(T_e)$ , which is given by

$$U_{\text{NT}} = \frac{3}{4} \rho \xi^2 \quad (4)$$

where  $\rho$  is the mass-density. This follows from the assumption that the non-thermal velocities follow a Maxwell-Boltzmann distribution in three dimensions, with most probably speed  $\xi$ . (See the Appendix for the cases of motions in one and two dimensions).  $\rho$  is given by

$$\rho = m_H \mu N_g \quad (5)$$

where  $m_H$  is the mass of hydrogen,  $N_g$  is the number density of all particles and  $\mu$  is the mean atomic weight defined as

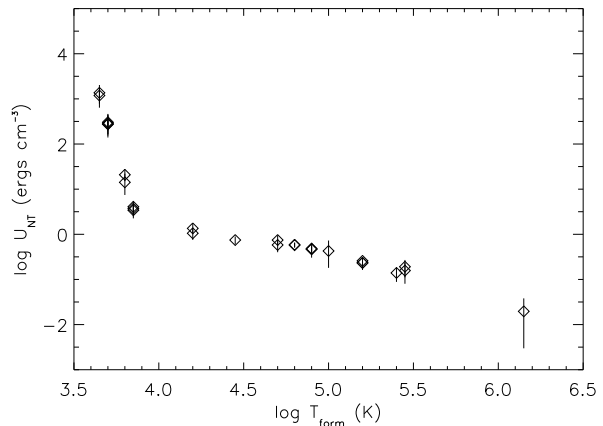
$$\mu = \frac{\sum_i m_i N_i}{m_H \sum_i N_i} \quad (6)$$

where  $m_i$  and  $N_i$  are the mass and number density of particles of species  $i$  in the plasma and the sums run over all such species. Adopting abundances similar to those in the solar photosphere,  $\mu$  can be approximated by

$$\mu \approx \frac{1.4 N_H}{N_e + 1.1 N_H} \quad (7)$$

where  $N_H$  is the number density of hydrogen and  $N_e$  is the electron number density. This gives  $\mu N_g \approx 1.4 N_H$ . Hence

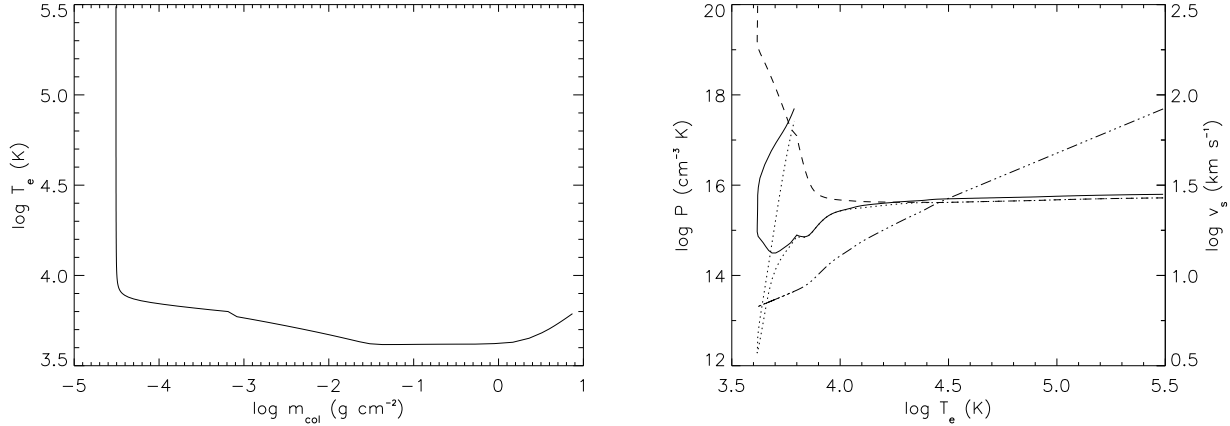
$$U_{\text{NT}} \approx 1.1 m_H N_H \xi^2. \quad (8)$$



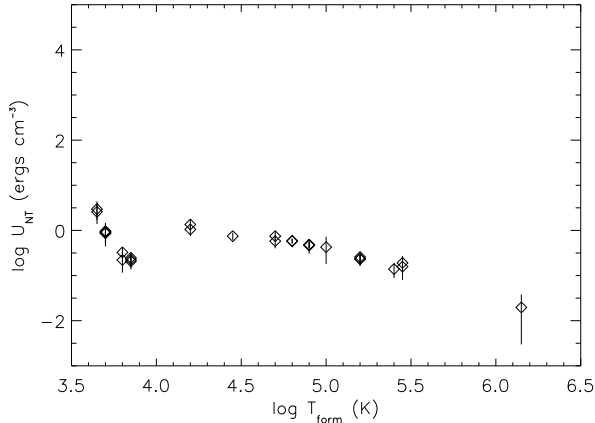
**Figure 2.** The non-thermal energy density in the gas plotted as  $\log U_{\text{NT}}$  versus  $\log T_{\text{form}}$ . The vertical bars show the uncertainty in  $U_{\text{NT}}$  due to the total uncertainty in  $\xi$ , but make no allowance for possible errors in  $\rho$ .

Fig. 2 shows a plot of  $U_{\text{NT}}$  in the gas against temperature.  $N_H$  has been taken from a semi-empirical model of the average atmosphere of  $\epsilon$  Eri (Sim 2002). The model is based on an emission measure distribution derived from line fluxes observed with STIS and the chromospheric model of Thatcher, Robinson & Rees (1991). This new model, and others, will be discussed in a forthcoming paper (Sim, in preparation). The important parameters in the model adopted here (column mass density, electron temperature, electron pressure, proton pressure, hydrogen pressure and sound speed) are shown in Fig. 3. The error bars in Fig. 2 give the total uncertainty in the values of  $\xi$ , but not the uncertainties in  $\rho$ . The form of  $U_{\text{NT}}$  with  $T_e$  is dominated by the variation of  $\rho$ , and is therefore considerably more sensitive to the adopted atmospheric model than to the measured values of  $\xi$  ( $\rho$  varies by more than five orders of magnitude across the temperature range in Fig. 2, compared to only a factor of three variation in  $\xi$ ). It is clear, however, that the non-thermal energy density in the chromosphere is at least three orders of magnitude greater than in the overlying transition region and corona.

When considering the propagation of waves which are coupled to the magnetic field (torsional Alfvén waves and fast mode waves when the Alfvén speed greatly exceeds the sound speed), the degree of ionization of the gas needs to be considered. This is relevant to the chromospheric regions where hydrogen is not fully ionized (see e.g. discussion in Osterbrock 1961). If the frequency of collisions between ions and neutrals is much larger than the wave frequency then there will be collisional coupling between the ions and neutral atoms, which can cause damping of the waves. In this case the gas density  $\rho$  is appropriate. Conversely, if the collision frequency is much less than the wave frequency, the ion density  $\rho_{\text{ion}}$  becomes the relevant density. The chromospheric model has been used to calculate  $\rho_{\text{ion}}$ , allowing for the protons, ‘metals’ with low first ionization potential, and the electrons produced by these and hydrogen (i.e. the ions and electrons are treated as a single fluid).  $\rho_{\text{ion}}$  is then given by



**Figure 3.** The adopted atmospheric model. The left-hand panel shows the electron temperature ( $T_e$ ) versus the mass column density ( $m_{\text{col}}$ ). The right-hand panel shows the electron (solid line), proton (dotted line) and total hydrogen (H and  $\text{H}^+$ , dashed line) pressures, and also the sound speed ( $v_s$ , triple-dot dashed line) versus  $T_e$ .



**Figure 4.** The non-thermal energy density in the ions plotted as  $\log U_{\text{NT}}$  versus  $\log T_{\text{ion}}$ . The vertical bars show the uncertainty in  $U_{\text{NT}}$  due to the total uncertainty in  $\xi$ , but make no allowance for possible errors in  $\rho_{\text{ion}}$ .

$$\rho_{\text{ion}} = m_e N_e + m_p N_p + m_m (N_e - N_p) \quad (9)$$

where  $m_e$  and  $m_p$  are the masses of the electron and proton, respectively,  $m_m$  is the mean mass of ions of elements other than hydrogen divided by the mean ionisation stage of such ions, and  $N_p$  is the proton number density.  $\rho_{\text{ion}}$  then replaces  $\rho$  in equation (4).

Fig. 4 shows the non-thermal energy density in the ions, which at  $T_e \leq 10^4$  K is significantly smaller than the total non-thermal energy density shown in Fig. 2. Since collisions between the ions and neutrals will occur and will transfer some energy to the neutrals, the actual relevant non-thermal energy density will lie between the extremes given by Figs. 2 and 4.

### 3.2 Wave Heating

We now consider the possibility that the non-thermal energy density is associated with waves propagating at either the

Alfvén speed or the sound speed, and examine the extent to which these hypotheses can account for the observations.

Provided the wave frequencies are sufficiently small (so that the WKB approximation is valid), and non-linear effects are small, the non-thermal energy flux,  $F_{\text{NT}}$ , is related to the kinetic energy density by

$$F_{\text{NT}} = 2U_{\text{NT}}v_{\text{prop}} \quad (10)$$

where  $v_{\text{prop}}$  is the appropriate propagation velocity and the factor of 2 accounts for equipartition of energy between kinetic and potential energies in the waves.

First we consider waves which propagate at the Alfvén speed, without distinguishing between torsional (shear) waves or compressional (fast-mode) waves when  $v_a \gg v_s$  (see Cross 1988 for Alfvén wave theory and references to early work). The formulation is given in terms of  $\rho_{\text{ion}}$ .

$$v_a = \frac{B}{\sqrt{4\pi\rho_{\text{ion}}}} \quad (11)$$

where  $B$  is the magnetic flux density.  $B$  is not known directly above the photosphere. Rüedi et al. (1997) have measured the spatially averaged surface magnetic flux density,  $B_0 = B_s A_s / A_*$ , where  $B_s A_s$  is the surface magnetic flux. They find a value of  $165 \pm 30$  G. In the overlying atmosphere we make the assumption that some fraction of the total stellar surface area is occupied by flux tubes, each with the same values of  $B$  and individual cross-sectional areas. Since not all the surface magnetic flux may continue through to higher layers, we specify the fraction which continue at a given  $T_e$  as  $b = BA / B_0 A_*$ , where  $A_*$  is the total surface area and  $A$  is the actual total surface area occupied by the magnetic field  $B$ , at given  $T_e$ . The observed spatially averaged non-thermal flux is then

$$\begin{aligned} F_{\text{NT}} \frac{A}{A_*} &= \frac{3}{2} \rho_{\text{ion}} \xi^2 v_a \frac{A}{A_*} \\ &= \frac{3}{2\sqrt{4\pi}} \rho_{\text{ion}}^{1/2} \xi^2 b B_0 \text{ erg cm}^{-2} \text{ s}^{-1} \end{aligned} \quad (12)$$

where  $F_{\text{NT}}$  refers to an individual flux tube. The factor 3, which was introduced in the calculation of the non-thermal

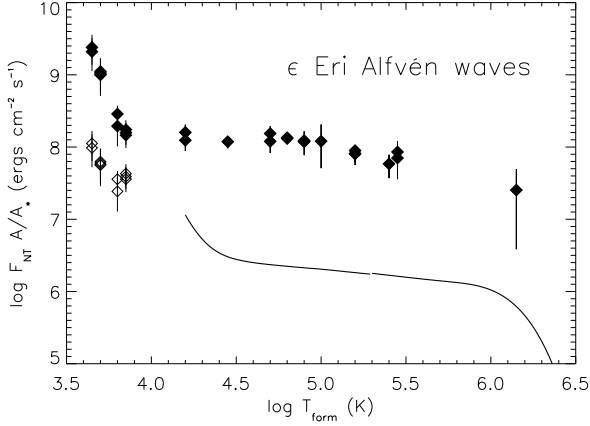


**Figure 5.**  $\log F_{\text{NT}} A/A_*$  versus  $\log T_{\text{form}}$  for Alfvén waves, adopting  $b = 1$ . The vertical error bars indicate the uncertainty in  $F_{\text{NT}}$  due to the total uncertainty in  $\xi$ ; no allowance is made for uncertainties in the values of  $\rho_{\text{ion}}$  in the atmosphere. The open symbols indicate the calculations using  $\rho_{\text{ion}}$  and the filled symbols show those with the total density  $\rho$ . The full line shows the flux required to account for the radiation losses above a given  $T_e$ .

energy density by the assumption of isotropic non-thermal motions in three dimensions, has been retained here. If the motion were in fact restricted to only 2 or 1 dimensions, as associated with purely transverse or longitudinal oscillations, equation (12) would overestimate the actual flux by factors of 1.5 and 3 respectively.

The spatially averaged non-thermal flux calculated using equation (12) and the observed value of  $B_0 = 165$  G is shown in Fig. 5, initially adopting  $b = 1$ . Results using  $\rho$  and  $\rho_{\text{ion}}$  are illustrated. The flux required to account for the radiation losses above a given  $T_e$  is also shown. The radiation losses have been calculated using the model shown in Fig. 3, which is based on the spatially averaged emission measure distribution derived by Sim (2002) and the radiative power losses of Cook et al. (1989), adopting the stellar photospheric abundances (which are similar to those of the Sun).

We also consider heating by acoustic waves propagating at the sound speed, given by

$$v_s = \left( \frac{\gamma k_B T_e}{\mu m_H} \right)^{1/2} \quad (13)$$

where  $\gamma = 5/3$  is the ratio of specific heats and  $T_e$  is the electron temperature. The mean molecular weight is given by equation (7). If the acoustic waves originate in some fraction of the surface area ( $A/A_*$ ), the corresponding spatially averaged non-thermal energy flux is

$$\begin{aligned} \frac{F_{\text{NT}} A}{A_*} &= \frac{3}{2} \rho \xi^2 v_s \frac{A}{A_*} \\ &\approx 4.1 \times 10^{-20} \xi^2 N_{\text{H}} \sqrt{\frac{T_e}{\mu}} \frac{A}{A_*} \text{ erg cm}^{-2} \text{ s}^{-1}. \end{aligned} \quad (14)$$

Fig. 6 shows the non-thermal flux assuming that the turbulent widths are due to the passage of acoustic waves with  $A/A_* = 1$ , and the flux required to account for the radiation losses above a given  $T_e$ . Above  $10^4$  K, the forms of

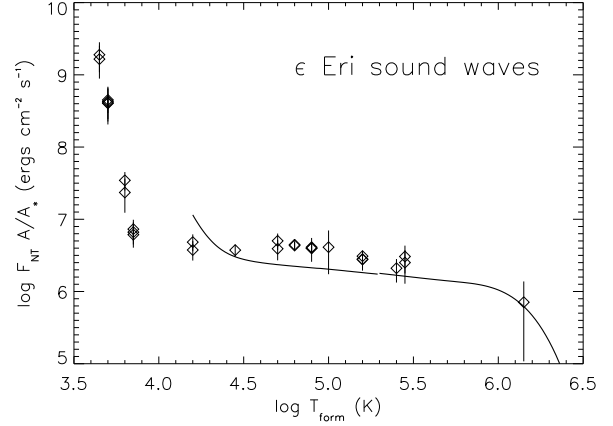


**Figure 6.**  $\log F_{\text{NT}}$  versus  $\log T_{\text{form}}$  for acoustic waves. The vertical error bars indicate the uncertainty in  $F_{\text{NT}}$  due to the total uncertainty in  $\xi$ , but do not attempt to estimate the uncertainty in the variation of  $\rho$  in the atmosphere. The full line shows the flux required to account for the radiation losses above a given  $T_e$ .

Figs. 5 and 6 are very similar; this is because, apart from the numerical constant, the only difference between equations (12) and (14) is the factor  $\sqrt{T_e(N_e + 1.1N_{\text{H}})} = \sqrt{P_g}$ . The pressure scale height is much greater than the thickness of the transition region and so  $P_g$  varies little between  $\log T_e = 4.0$  and  $\log T_e = 6.0$ . However  $P_g$  increases rapidly below  $T_e \simeq 10^4$  K, which is why Fig. 6 displays a steeper gradient in the chromosphere.

The form of the curves in Figs. 5 and 6 show that in both cases the non-thermal wave flux is roughly constant between  $\log T_e = 4.2$  and 4.8, consistent with a transport of non-thermal energy with little dissipation. This apparent constancy of the wave flux also shows up in Fig. 1, since over this range of temperature  $\xi$  is approximately  $\propto T_e^{1/4}$ , as in the solar transition region (Jordan 1991). This gradient is expected if there is a constant Alfvén wave flux (in the WKB approximation), or a constant acoustic flux, provided the electron pressure and  $b$  are constant. Under the same circumstances a constant turbulent energy flux would give  $\xi \propto T_e^{1/3}$ . At higher temperatures,  $\xi$  is roughly constant and then decreases, so  $F_{\text{NT}}$  appears to decrease. This could occur if energy is being dissipated (but see below). It is not surprising that  $\xi$  hardly varies over the mid-transition region. The temperature gradient in the spatially averaged models is large (as in the Sun), so the range of  $T_e$  involved corresponds to a small height difference (less than 100 km).

In the case of an acoustic energy flux it is possible that the decrease above  $10^5$  K is simply a geometrical effect; the area occupied by the regions associated with the acoustic flux could increase with  $T_e$ . The flux shown in Fig. 6 is the spatially averaged value, with the term  $A/A_*$  on the r.h.s of equation (14) taken as 1. An increase in  $A/A_*$  from a low value in the transition region to a larger value in the corona could lead to  $F_{\text{NT}} A/A_*$  being constant until dissipation occurs in the corona.

Simple energy requirement arguments can probably rule out coronal heating by acoustic waves. From Fig. 6 the acoustic energy flux passing into the corona at  $T_e \simeq 1.4 \times 10^6$  K is  $\approx 8 \times 10^5$  ergs  $\text{cm}^{-2} \text{ s}^{-1}$ , assuming that



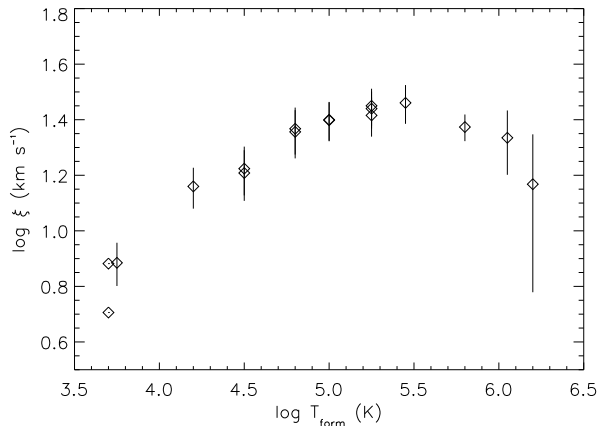


**Figure 7.**  $\log \xi$  versus  $\log T_{\text{form}}$  from the solar data of Chae et al. (1998).

$A/A_* = 1$  by this temperature. Although this could account for the coronal radiation losses, it is significantly smaller than the estimated energy loss by thermal conduction at  $1.4 \times 10^6$  K ( $\sim 3 \times 10^6$  erg cm $^{-2}$  s $^{-1}$ , according to Jordan et al. 2001a). Also, there is insufficient flux below  $\simeq 2 \times 10^4$  K. Thus the simple acoustic model appears to be unable to provide enough energy to heat the corona of  $\epsilon$  Eri.

For an Alfvén wave flux the argument concerning the area factor fails because the factor  $b$  in equation (12) can only be constant or *decrease* with  $T_e$ . There is ample energy flux to account for the energy losses from the corona if  $b = 1$  (i.e. all the surface magnetic flux extends to the corona). Indeed, only around 20 per cent of the surface magnetic flux need extend to the corona to match the estimated energy flux lost by thermal conduction at, and radiation losses above,  $1.4 \times 10^6$  K ( $\simeq 4 \times 10^6$  erg cm $^{-2}$  s $^{-1}$ ). With the fluxes shown in Fig. 5 difficulties occur with the decrease in  $F_{\text{NT}}A/A_*$  above  $10^5$  K. This decrease could be interpreted as being due to energy dissipation in the upper transition region, which could in principle be balanced by radiation losses and thermal conduction. However, including a heating process in addition to radiation losses will act to increase the gradient of the theoretical emission measure distribution (EMD) (see Jordan 2000). To match the decrease in  $F_{\text{NT}}A/A_*$ , apparent above  $10^5$  K in Fig. 5, would require the gradient of the observed EMD to be at least an order of magnitude greater than that derived from line fluxes. Thus an interpretation of the fluxes in Fig. 5 in terms of heating in the upper transition region is not viable. If  $b$  is less than 1, then this constraint is less demanding.

The radiation losses shown in Figs. 5 and 6 ignore the role played by thermal conduction above  $T_e \simeq 2 \times 10^5$  K. If the thermal conduction leaving the corona is balanced by the local radiation losses, then no additional heating is required between  $2 \times 10^5$  K and the base of the corona. Over this temperature range, when comparing with the heating flux, one needs to consider only the conductive flux and radiation lost from the corona, with further radiation losses being added below  $2 \times 10^5$  K.

The heating requirements of the chromosphere can also be considered. First we consider an acoustic flux. The form of Fig. 6 shows that if the turbulent velocities are associated

with propagating waves a substantial fraction of the total non-thermal energy would be deposited in the low chromosphere. The non-thermal energy flux would have to decrease by  $\sim 10^9$  ergs cm $^{-2}$  s $^{-1}$  across the low chromosphere. This far exceeds any reasonable estimate of the radiative losses from this region. Linsky & Ayres (1978) estimated that in cool main-sequence stars, the radiative fluxes in the Mg II h & k lines are comparable to 30 per cent of the total radiative flux from the chromosphere. The total observed flux at the Earth in the Mg II h and k lines in  $\epsilon$  Eri (in our STIS spectra) is around  $5.4 \times 10^{-11}$  erg cm $^{-2}$  s $^{-1}$ , corresponding to a stellar surface flux of  $1.7 \times 10^6$  erg cm $^{-2}$  s $^{-1}$ . This gives an estimated total surface radiative flux from the chromosphere of  $8.8 \times 10^6$  ergs cm $^{-2}$  s $^{-1}$ . Although only a crude estimate, this shows that far too much energy would be dissipated in the low chromosphere if the observed non-thermal motions are interpreted in terms of a propagating acoustic wave flux.

If we invoke an area filling factor, then in the chromosphere,  $A/A_*$  would have to be much lower than at  $10^4$  K, and would need to increase rapidly by around  $10^4$  K. This seems unlikely, as in the Sun, acoustic waves are thought to be important only in the interiors of supergranulation cells, whose area does not change significantly in the overlying regions. By analogy with the solar chromosphere, the spatially integrated emission and the observed line widths are likely to be dominated by the contribution from the supergranulation boundaries. In this case, relating the line widths to acoustic waves will not be correct, and the apparent discrepancy between the observed and deduced fluxes is understandable.

From the limits to the Alfvén wave flux shown in Fig. 5 it is clear that there is no difficulty in principle in obtaining sufficient flux to pass through to the lower transition region and the flux around  $2 \times 10^4$  K represents an upper limit available to the overlying regions. We do not address the question of how the supergranulation boundary regions in the chromosphere are heated. (Osterbrock 1961 gives a discussion of the possible processes involved, but with numerical values of parameters that require revision in the light of modern measurements of magnetic fields and current chromospheric models).

In Fig. 7 we show the non-thermal velocities calculated using the solar line widths given by Chae et al. (1998). Fig. 8 shows the non-thermal wave fluxes calculated from equations (12) and (14) using these non-thermal velocities and densities taken from model C (average quiet Sun) of Vernazza, Avrett, & Loeser (VAL) (1981). Again, the upper and lower limits on the Alfvén wave fluxes are shown. As in Fig. 5,  $b$  has been set to 1.0. The adopted temperatures of line formation are similar to those used by Chae et al. (1998), except for the neutral chromospheric lines. For these lines significantly lower values of  $T_{\text{form}}$  have been used, based on radiative transfer calculations with the VAL-C (1981) model. These lower temperatures lead to a difference in the dependence of the fluxes with  $T_e$ , when comparisons are made with the calculations by Chae et al. (1998) (their fig. 13). The mean magnetic flux density was taken as 20 Gauss (see discussion in Montesinos & Jordan 1993). Apart from the absolute scales, the variations of the spatially averaged fluxes are quite similar to those found for  $\epsilon$  Eri: for Alfvén waves the lower limit to the chromospheric flux is similar to the flux in the lower transition region, while for acoustic waves and the upper limit to the Alfvén wave flux, there is a large

drop in  $F_{\text{NT}}$  between the chromosphere and transition region. In both cases the flux is almost constant through the low transition region with a decrease in the upper transition region. In the Sun, the factor by which the flux decreases in the upper transition region is larger than in  $\epsilon$  Eri, but begins at a slightly higher temperature. The presence of a dip at around  $\log T_e = 4.5$  relies heavily on the accuracy of the non-thermal contribution to the line-width of the optically thick C II lines deduced by Chae et al. (1998).

It is surprising that in the Sun, and in  $\epsilon$  Eri, in the low transition region  $\xi$  increases according to  $T_e^{1/4}$ , consistent with a constant Alfvén wave energy flux in the WKB approximation. This approximation is valid only if the wavelength is less than the scale-height of the Alfvén wave speed (see e.g. Meyer 1976; Hollweg 1991 and references therein); i.e. if the Alfvén wave period  $\tau_w$  is such that

$$\tau_w \ll \frac{2\pi}{v_a} 2H \quad (15)$$

where  $H$  is the scale-height of the Alfvén speed. If  $\tau_w$  is much larger than this value, then the waves become evanescent and  $\xi$  would be constant with height (which is observed to occur around  $10^5$  K). Defining  $H = v_a(dh/dv_a)$ , the critical period can be expressed as

$$\tau_c = \frac{2.0 \times 10^{-10} Em(0.3)_t T_e^{3/2}}{BP_e^{3/2} (0.5 + \frac{d \log B}{d \log T_e})} \quad (16)$$

where the temperature gradient has been written in terms of the true (intrinsic) emission measure and the electron pressure ( $P_e = N_e T_e$ ), i.e.

$$Em(0.3)_t = \frac{P_e P_H}{\sqrt{2} T_e} \frac{dh}{dT_e} \quad (17)$$

For a plane parallel layer  $Em(0.3)_t$  can be replaced by  $2Em(0.3)_{obs} A_*/A$ . As before,  $BA$  is replaced by  $B_o A_* b$ , and the unknown area  $A$ , but not its variation with  $T_e$ , cancels. Working above  $\simeq 2 \times 10^4$  K (since we take  $P_e$  and  $\mu$  to be constant) the critical period can be found as a function of  $T_e$ , provided assumptions are made about  $b$  and the change in the area factor  $A$ . I.e.

$$\tau_c = \frac{2.0 \times 10^{-10} Em(0.3)_{obs} T_e^{3/2}}{B_o b P_e^{3/2} [0.5 + \frac{d \log(b/A)}{d \log T_e}]} \quad (18)$$

Since the area occupied by the solar supergranulation network varies little through the low to mid transition region, we assume that  $A$  is constant and we have to assume that  $b = 1$ . For the Sun, using  $B_0 = 20$  G,  $P_e = 2.1 \times 10^{14} \text{ cm}^{-3} \text{ K}$ , and the network values of  $Em(0.3)_{obs}$  from Macpherson & Jordan (1999), the values of  $\tau_c$  are  $\simeq 20$  s at  $2 \times 10^4$  K,  $\simeq 4$  s at  $8 \times 10^4$  K, and increase again to  $\simeq 30$  s at  $3 \times 10^5$  K. For the assumed parameters these are minimum values since only a small increase in  $A$  with  $T_e$  will increase  $\tau_c$ , and if  $b$  is less than 1, and decreases with  $T_e$ , this will also increase  $\tau_c$ . Also, the value of  $B_0$  used could be a factor of 2 smaller. Thus although the critical wave periods are short, it is not certain that WKB waves can be excluded. The most stringent condition occurs around  $8 \times 10^4$  K, where (maybe coincidentally)  $\xi$  begins to increase by a power of  $T_e$  which is less than  $1/4$ . In  $\epsilon$  Eri, the values of  $Em(0.3)_{obs}$ ,  $P_e$  and  $B_0$  are all larger, but result in values of  $\tau_c$  that are smaller by a factor of about 130, with the same trends with  $T_e$ . The values of  $b$  and  $d \log(b/A)/d \log T_e$ , which act to increase

the critical period, therefore become the crucial factors in deciding whether or not the waves can satisfy the WKB approximation.

As Hollweg (1991, and references therein) has stressed, if the WKB approximation does not hold, then the energy flux carried can be larger or smaller than that deduced by using the approximation. There is also the possibility of wave reflection by the steep Alfvén wave gradient, and wave propagation at particular frequencies (resonances). Together, in principle, these effects might account for the apparent decrease in the Alfvén wave flux that appears in Figs. 5 and 8, without invoking wave dissipation in the upper transition region. If wave reflection occurs, there is also the possibility that eventual wave dissipation could contribute to the heating of the lower transition region. Although we do not attempt an analysis of possible wave processes, the new observations of  $\epsilon$  Eri, and the new models being produced, will place strong constraints on future detailed calculations of wave propagation through the transition region.

#### 4 LINE SHIFTS

Unless otherwise stated, the rest wavelengths given in Table 3 are taken from Kurucz & Bell (1995). In general, these agree with those given by Kelly (1987) to within  $0.001 \text{ \AA}$ . In Jordan et al. (2001a) we noted that the wavelength interval between the two lines of N V is slightly larger than that given by the values from Kelly (1987) (which are the same as in Kurucz & Bell 1995, and originate from laboratory measurements by Hallin 1966). There has been previous debate concerning the N V wavelengths in the Sun (see Achour et al. 1995; Brekke, Hassler & Wilhelm 1997, and references therein). Brekke et al. (1997) find that for the  $1242.8\text{-\AA}$  line the best agreement is with the measurement by Hallin (1966) ( $1242.804 \text{ \AA}$ ). For the  $1238.8\text{-\AA}$  line, they find best agreement with the earlier measurement by Edlén (1934) ( $1238.800 \text{ \AA}$ ). Combining these wavelengths gives a wavelength interval of  $4.004 \text{ \AA}$ . Of the various combinations of the laboratory wavelengths this one does give the best agreement with our interval of  $3.994 \text{ \AA}$ , which should be accurate to within  $0.007 \text{ \AA}$ , and appears to be the best measurement of the interval to date. Since we do not have absolute wavelengths, we use the values by Hallin (1966) in Table 3, but point out that the  $1242.804\text{-\AA}$  line is likely to give more accurate wavelength shifts. Our measured interval suggests that the wavelength of the other line should be  $1238.810 \text{ \AA}$ . It would be useful to remeasure these wavelengths in the laboratory with modern techniques.

New interferometric measurements of lines from the alkali-like ions C IV and Si IV are available from the work of Griesmann and Kling (2000), and these are adopted in Table 3. For C IV the new values agree more closely with the values of Kelly (1987) than with those in Kurucz & Bell (1995) and lead to smaller observed red-shifts. The wavelength interval between the two C IV lines that we measure is definitely smaller than that given in Kurucz & Bell (1995), and agrees most closely with that from the wavelengths given by Kelly (1987). For the Si IV lines our measured interval is consistent with those listed in all the above three papers. The new measurement by Griesmann & Kling (2000) for the line of Al II is also adopted in Table 3, although it is not significantly

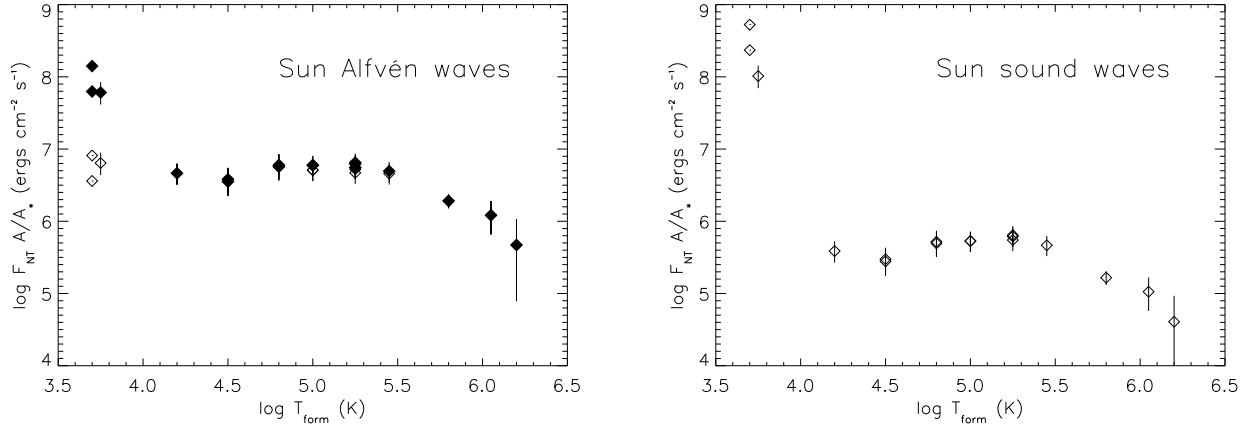


**Figure 8.**  $\log F_{NT}$  versus  $\log T_{form}$  from the solar data of Chae et. al (1998). The left-hand panel is for Alfvén waves and the right-hand panel is for acoustic waves. In the left-hand panel the open symbols indicate the calculations using  $\rho_{ion}$  and the filled symbols show those with the total density  $\rho$ .

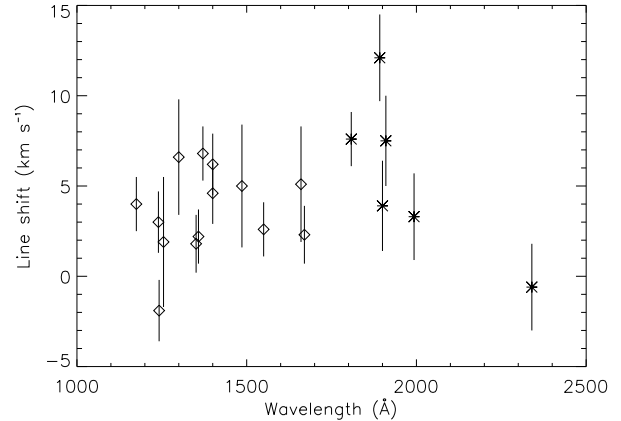
different from the earlier value, given the uncertainty in the observed value.

The wavelength calibration of *FUSE* is not accurate, so no absolute wavelengths can be measured for the O VI and C II 1037-Å mult. lines. Since these lines are all close together in wavelength, their relative wavelengths can be measured. The wavelength interval between the O VI lines agrees with the values in both Kurucz & Bell (1995) and Kelly (1987) to within our measurement uncertainty of 0.025Å. That between the C II lines agrees with the laboratory measurements for this spectroscopic standard, to within our measurement uncertainty. There is then no relative shift between the O VI lines and the C II lines (which are formed where the mean red-shift is 2–7 km s<sup>-1</sup>), to within the measurement uncertainty of  $\simeq 4$  km s<sup>-1</sup>, it appears that the red-shifts of the O VI lines are no greater than that of O V.

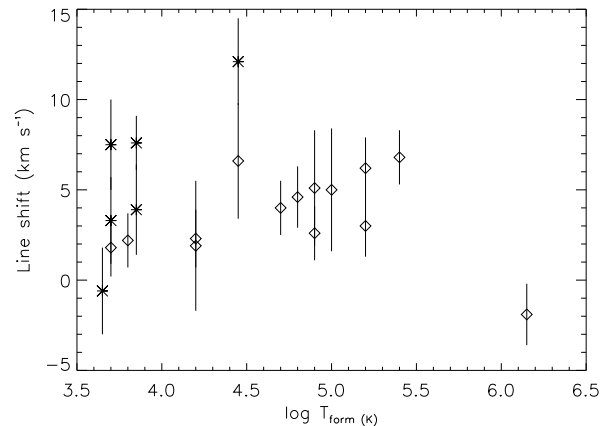
The line shifts given in Table 3 are plotted as a function of wavelength in Fig. 9 and of temperature of formation in Fig. 10. The diamonds indicate lines observed with the E140M grating and the asterisks those which are observed with the lower resolution E230M grating. For multiplets in which the individual line shifts agree to within the measurement errors (see Table 3) the individual shifts have been combined to give a single shift for the multiplet.

Fig. 9 shows that most of the lines display a small (few km s<sup>-1</sup>) red-shift, although the scatter is quite large. There appears to be an offset in the wavelength calibration of the E230M grating (which covers the wavelength range  $\lambda > 1750$  Å) compared with that of the E140M grating, since at a given  $T_e$ , the lines observed around 1800 Å to 1900 Å observed with the E230M grating show larger redshifts than those observed with the E140M grating. The offset is small and corresponds to only about 2 pixels in wavelength, but in the discussion below we restrict our comments to the trends in the E140 data.

Fig. 10 does not show a strong trend in the line shifts with  $T_{form}$ . Using only the lines observed with the E140M grating, the mean red-shift is  $3.7 \pm 0.6$  km s<sup>-1</sup>. The mean red-shift of the mid transition region lines ( $4.4 < \log T_{form} < 5.5$ ) is  $4.9 \pm 0.8$  km s<sup>-1</sup> while that for the lower temperature lines



**Figure 9.** Line shift versus wavelength. The lines observed with the E140M grating are shown by  $\diamond$ , and those observed with the E230M grating by  $*$ .



**Figure 10.** Line shift versus  $\log T_{form}$ . Symbols as in Fig. 9.

**Table 4.** Fit parameters from two-Gaussian fits to selected strong lines.  $F$  denotes the integrated line flux, given in  $10^{-13}$  ergs  $\text{cm}^{-2}$   $\text{s}^{-1}$  at the Earth. The subscripts N and B denote “Narrow” and “Broad” components respectively. The errors are formal  $1\sigma$  errors deduced from the correlation matrix of each fit.

Ion	$\lambda_0(\text{\AA})$	$F_N$	$\Delta\lambda_N(\text{\AA})$	$\lambda_{\text{obs},N}(\text{\AA})$	$F_B$	$\Delta\lambda_B(\text{\AA})$	$\lambda_{\text{obs},B}(\text{\AA})$
C IV	1548.204	$3.293 \pm 0.152$	$0.165 \pm 0.004$	$1548.221 \pm 0.001$	$2.177 \pm 0.137$	$0.420 \pm 0.019$	$1548.247 \pm 0.004$
C IV	1550.781	$1.396 \pm 0.108$	$0.147 \pm 0.007$	$1550.784 \pm 0.002$	$1.453 \pm 0.103$	$0.372 \pm 0.016$	$1550.805 \pm 0.004$
N V	1238.821	$0.676 \pm 0.062$	$0.151 \pm 0.008$	$1238.828 \pm 0.002$	$0.304 \pm 0.058$	$0.377 \pm 0.047$	$1238.845 \pm 0.009$
N V	1242.804	$0.334 \pm 0.051$	$0.147 \pm 0.011$	$1242.817 \pm 0.003$	$0.145 \pm 0.047$	$0.332 \pm 0.062$	$1242.865 \pm 0.028$
O VI	1031.912	$3.540 \pm 0.136$	$0.173 \pm 0.003$	$1031.940 \pm 0.001$	$1.065 \pm 0.127$	$0.376 \pm 0.022$	$1031.959 \pm 0.005$
O VI	1037.613	$1.858 \pm 0.074$	$0.170 \pm 0.004$	$1037.615 \pm 0.001$	$0.417 \pm 0.067$	$0.392 \pm 0.035$	$1037.630 \pm 0.006$
Si III	1892.030	$0.794 \pm 0.089$	$0.158 \pm 0.012$	$1892.105 \pm 0.004$	$0.523 \pm 0.093$	$0.427 \pm 0.042$	$1892.112 \pm 0.022$
Si IV	1393.760	$1.285 \pm 0.050$	$0.136 \pm 0.004$	$1393.780 \pm 0.001$	$0.960 \pm 0.047$	$0.379 \pm 0.012$	$1393.793 \pm 0.003$
Si IV	1402.773	$0.739 \pm 0.038$	$0.141 \pm 0.005$	$1402.794 \pm 0.002$	$0.450 \pm 0.034$	$0.427 \pm 0.026$	$1402.803 \pm 0.006$

is  $2.1 \pm 1.1$   $\text{km s}^{-1}$ . Thus, on average, the lower temperature lines are less red-shifted by about  $3$   $\text{km s}^{-1}$ . The Fe XII line is apparently blueshifted, but this relies on the solar wavelength at the limb.

In the solar transition region, using spatially integrated observations at Sun-centre, Peter & Judge (1999) found red-shifts of up to  $9.9$   $\text{km s}^{-1}$  in the N V lines, and smaller red-shifts in lines formed at lower and higher temperatures. These red-shifts decrease towards the limb. For the Si IV, C IV and N V lines in common with our observations of  $\epsilon$  Eri, we find similar red-shifts (if we adopt the wavelengths from Kurucz & Bell 1995), except for the N V lines, for which our values are significantly smaller. The new wavelengths we adopt for Si IV and C IV do, however, lead to smaller red-shifts (see Table 3). If the Fe XII wavelength is reliable, then like Peter & Judge (1999) we observe a blue-shift in the Fe XII line, although this is smaller in  $\epsilon$  Eri.

The physical origin of the shifts is not yet understood, although it has been suggested by Hansteen (1993) that these could be due to waves propagating *downwards* from reconnection events (nanoflares) in the corona, or in the mid transition region (Peter & Judge 1999). However, our line-width measurements, using one-Gaussian fits, show no evidence that the energy flux *increases* with temperature, as one would expect if the origin of the waves was within the corona. In the solar photosphere the velocity fields associated with the supergranulation flow are very small, but the possibility of convective overshoot into the transition region, and resulting downflows in the cell boundaries, does not appear to have been investigated. With lower densities and mass conservation, larger velocities are in principle possible at the level of the transition region. It is also interesting that, in at least one solar boundary region, Macpherson, Jordan & Smith (1999) found that the downflows appear to be adjacent to, rather than in, the brightest regions of the boundaries. Overall, the origin of the red-shifts is still not understood.

As discussed above, in stellar observations only the combined effects of red- and blue-shifts can be observed, which could contribute to the line widths. The shifts observed are significant compared with the uncertainty of  $0.9$   $\text{km s}^{-1}$  in the stellar radial velocity. The shifts derived from two-component fits to line profiles are discussed below in Section 5.

## 5 TWO-COMPONENT FITS

It has previously been found (see Section 1) that the profiles of some transition region lines are described better by a two-Gaussian fit than a one-Gaussian fit. This has been taken as an indication that there are (at least) two separate atmospheric components contributing to the line emission. This two-component nature of line widths has been studied in the Sun (Peter 2000a,b; 2001) and other stars (Wood et al. 1997). These authors have found that line profiles for strong lines are described well by a sum of two Gaussians, one narrow and one broad. For the Sun, Peter (2000a,b; 2001) found that the presence of the second, broad component is restricted to the bright supergranulation network boundaries and that the cell interior regions show only the narrow component.

The excellent resolution and high signal-to-noise of the  $\epsilon$  Eri STIS spectra allow reliable two-component fits to be made to several of the strong spectral lines. The lines for which two-component fits have been made (these were selected on the grounds that they are sufficiently strong to reliably identify a second component) are listed in Table 4, which also gives the flux ( $F$ ), wavelength ( $\lambda_{\text{obs}}$ ) and width ( $\Delta\lambda$ ) for both the narrow and broad components. The error estimates quoted in Table 4 are formal  $1\sigma$  errors derived from the covariance matrix of the fit. The fluxes and widths are all strongly correlated while (with the exception of the N V 1242- $\text{\AA}$  line) the wavelengths are only weakly correlated with the other parameters. Errors estimated this way do not explicitly include the limitation on measuring wavelengths due to the instrumental resolution, so the true uncertainties in  $\lambda_{\text{obs}}$  are larger than estimated here for the narrow components, and are similar to the errors in  $\lambda_{\text{obs}}$  as given in Table 1. Based on the line lists of Kurucz & Bell (1995) and Sandlin et al. (1986), no significant blends are expected in the wavelength ranges over which the fits to the profiles have been made.

For the strong lines, a two-component fit gives a significantly better description of the data than does a one-component fit. To illustrate this, Fig. 11 shows the observed C IV, Si IV, N V, O VI and Si III (1892- $\text{\AA}$ ) lines with single-Gaussian fits and residuals (left-hand panels) and with double-Gaussian fits and residuals (right-hand panels). By examining the residuals it is clear that the two-component fit gives a substantial improvement for the C IV and Si IV lines and some improvement for the other lines. To

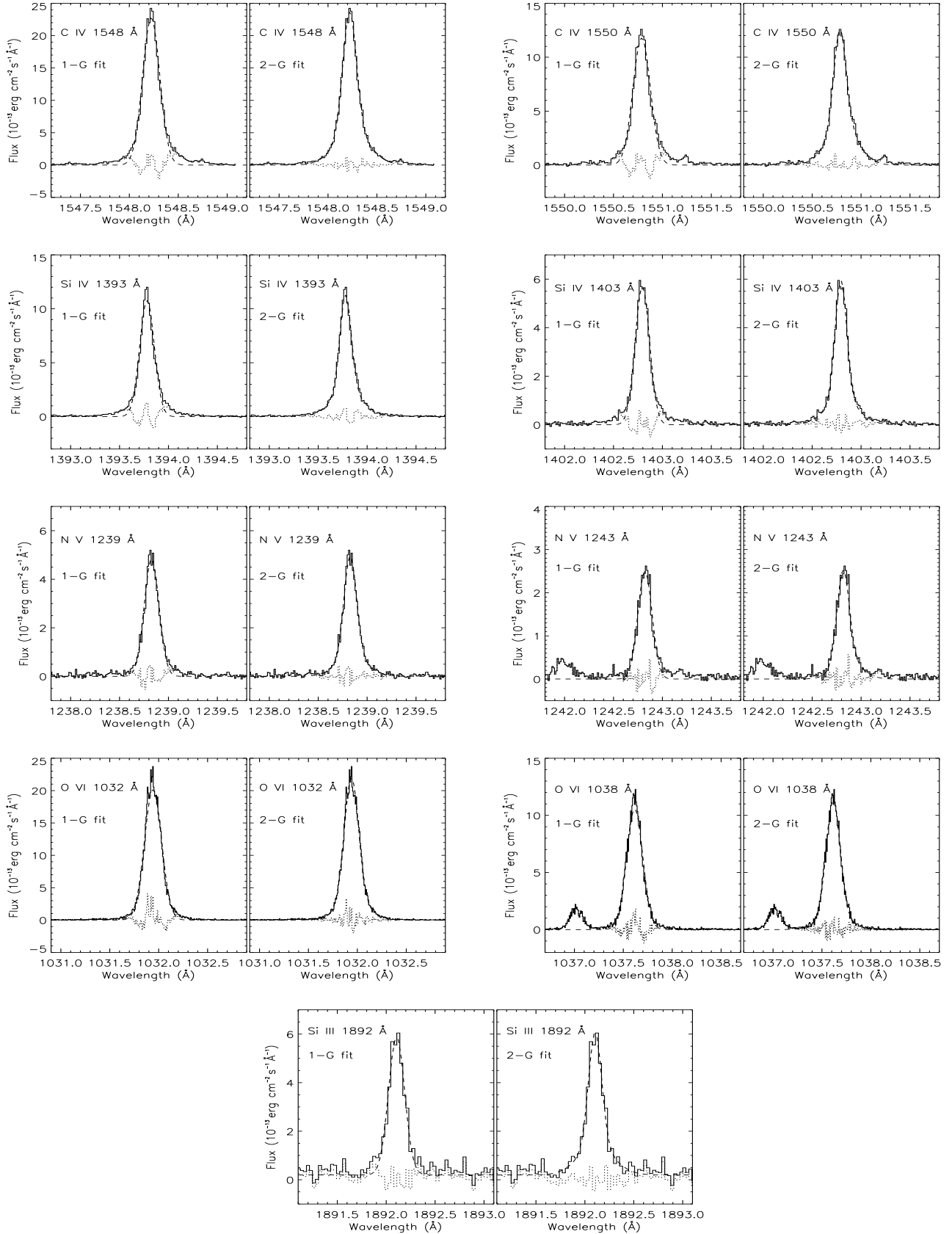


**Figure 11.** Comparison of one-Gaussian fit (left) and two-Gaussian fit (right) for (from top left) the C IV 1548-Å and 1550-Å lines, the Si IV 1393-Å and 1402-Å lines, the N V 1238-Å and 1242-Å lines, the O VI 1032-Å and 1038-Å lines and the Si III 1892-Å line. The observed profiles are shown by the solid line, the fits by the dashed lines and the residuals by the dotted lines.

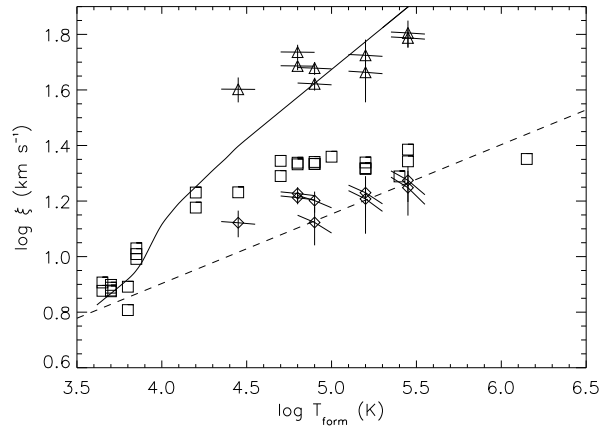
**Table 5.** Reduced chi-squared ( $\chi_r^2$ ) for one- and two-Gaussian fits to selected strong lines.

Ion	$\lambda_0$ (Å)	$\chi_r^2$ (one-Gaussian)	$\chi_r^2$ (two-Gaussian)
C IV	1548.204	14.28	0.87
C IV	1550.781	8.24	1.40
N V	1238.821	2.18	0.80
N V	1242.804	2.20	1.22
O VI	1031.912	5.25	1.34
O VI	1037.613	3.11	1.18
Si III	1892.030	1.70	0.89
Si IV	1393.760	18.04	2.18
Si IV	1402.773	6.67	1.06

be more quantitative, the one- and two-Gaussian fits have been used to calculate the reduced chi-squared ( $\chi_r^2$ ) statistic for each of the lines considered; these are given in Table 5 and show that the two-Gaussian fits give a significantly better description of the profiles than do the one-Gaussian fits. The reduction in  $\chi_r^2$  is greatest for the C IV and Si IV lines but is still large enough to strongly suggest the presence of a second component in the N V, O VI and Si III lines.

As for the one-Gaussian fit parameters, the two-Gaussian fit parameters (and associated  $1\sigma$  errors) have been converted to velocity shifts ( $v$ ) and most probable turbulent velocities ( $\xi$ ) for both components of each line. The results are given in Table 6. The temperatures at which both components are formed have been assumed to be the same as that used for the one-Gaussian fits. The uncertainty in  $\xi$  allows for a  $\pm 0.1$  dex uncertainty in  $\log T_{\text{form}}$  in the same way as adopted for the one-Gaussian fits. For O VI no velocity shift is given for the narrow component owing to the uncertainty in the *FUSE* wavelength calibration. The velocity shift given for the broad component is that relative to the narrow component.

The red-shifts found for the narrow components are essentially the same as those found for the one-Gaussian fits. A significant difference between the present results and the solar results found by Peter (2000a,b; 2001) is that in  $\epsilon$  Eri the broad component is *red-shifted* relative to the narrow component, typically by about  $4 \text{ km s}^{-1}$ . This can be seen directly in the asymmetry of the residuals shown in Fig. 11. Peter (2000a) found that in observations of C IV near Sun-centre the narrow component in the supergranulation cell boundaries is usually red-shifted, but the broad component is red-shifted *less*. However, in Peter's (2000a) detailed plots, there are a significant number of points where the red-shift of the broad component exceeds that of the narrow component, although these tend to occur when the intensity of the broad component is small. Since the relative intensity of the broad component in  $\epsilon$  Eri is larger than in the Sun (see below), this trend acts in the wrong direction to account for our results. In the cell interiors, where the broad component is absent, the profiles show red-shifts comparable to those of the narrow components in the boundaries. In stellar observations of the C IV lines Wood et al. (1997) observe a relatively greater red-shift of the broad component in the M-type flare star AU Mic, but this line was not observed in the other less active main-sequence stars  $\alpha$  Cen A and B. However, in all three stars the Si IV lines show relative shifts

**Figure 12.**  $\log \xi$  versus  $\log T_{\text{form}}$  for the 2-component fits (broad components shown by triangles; narrow components shown by diamonds). The single-component fits are shown by squares. The full line shows the sound speed and the dashed line shows a gradient of  $\xi \propto T_{\text{form}}^{-1/4}$ , with an amplitude normalized to the O VI narrow component.

in the same sense as in the Sun, in contrast to our results for  $\epsilon$  Eri.

Fig. 12 shows the non-thermal velocities of the two components as a function of the line formation temperature. For comparison, the single component points are shown again. The solid line shows the sound speed. The dashed line shows a gradient corresponding to  $\xi \propto T_{\text{form}}^{-1/4}$ , normalized to pass through the O VI narrow components.

The width of the broad component gives non-thermal velocities which are greater than the sound speed for the Si III and Si IV lines, close to the sound speed for C IV and significantly below the sound speed for N V. This behaviour is similar to that found by Peter (2001) for the Sun and for the high gravity stars studied by Wood et al. (1997). The widths of the low temperature lines from the single-Gaussian fits are also close to the sound speed (see Fig. 1 for the error bars).

As in the Sun (Peter 2001), the ratio of the non-thermal widths of the two components is almost constant. The mean ratio in  $\epsilon$  Eri is about 3, larger than the solar value (for lines in common) of about 2. Although the non-thermal widths of the broad components in  $\epsilon$  Eri are on average similar to those in the Sun, the widths of the narrow component are smaller in  $\epsilon$  Eri, by about a factor of 1.3. Wood et al. (1997) found a systematic decrease in the width of the C IV and Si IV narrow components with increasing surface gravity. These widths in  $\epsilon$  Eri fit their proposed relation  $\xi \propto g_*^{-0.68 \pm 0.07}$  remarkably well. A dependence on  $g_*$ , or alternatively the gas pressure, could indicate that turbulent motions are ultimately involved in any wave generation. Peter (2001) suggests that the broad component corresponds to a constant Alfvén wave flux, with  $\xi \propto T_{\text{form}}^{1/4}$ . In  $\epsilon$  Eri, to within the uncertainties, the same form would fit both components up to  $T_e \simeq 3 \times 10^5$  K. As stressed above, the temperature dependence expected for  $\xi$  depends on the details of the wave periods and any departures from the WKB approximation.

Peter (2001) found that the relative fluxes in the narrow and broad components vary with temperature, with

**Table 6.** Line shifts ( $v$ ) and turbulent velocities ( $\xi$ ) for two-component fits. The subscripts N and B denote “Narrow” and “Broad” components respectively. The errors are deduced from the  $1\sigma$  errors in Table 4 and are given in same format as those in Table 2.

Ion	$\lambda_0$ (Å)	$v_N$ (km s $^{-1}$ )	$\xi_N$ (km s $^{-1}$ )	$v_B$ (km s $^{-1}$ )	$\xi_B$ (km s $^{-1}$ )
C IV	1548.204	$+3.3 \pm 0.2$	$15.91^{+1.23(0.69)}_{-1.52(0.92)}$	$+8.3 \pm 0.8$	$47.70^{+2.49(0.24)}_{-2.58(0.30)}$
C IV	1550.781	$+0.6 \pm 0.4$	$13.27^{+1.80(0.82)}_{-2.29(1.11)}$	$+4.6 \pm 0.8$	$41.88^{+2.17(0.27)}_{-2.28(0.34)}$
N v	1238.821	$+1.7 \pm 0.5$	$16.98^{+2.50(1.10)}_{-3.19(1.49)}$	$+5.8 \pm 2.2$	$53.05^{+7.36(0.36)}_{-7.64(0.46)}$
N v	1242.804	$+3.2 \pm 0.7$	$16.13^{+3.09(1.15)}_{-4.04(1.58)}$	$+14.7 \pm 6.8$	$46.09^{+9.67(0.42)}_{-10.16(0.53)}$
O VI	1031.912	see text	$18.82^{+2.30(1.53)}_{-3.09(2.12)}$	$+5.5 \pm 1.7$	$61.28^{+4.54(0.49)}_{-4.80(0.62)}$
O VI	1037.613	see text	$17.70^{+2.66(1.62)}_{-3.65(2.28)}$	$+4.3 \pm 2.0$	$63.86^{+6.87(0.47)}_{-7.19(0.59)}$
Si III	1892.030	$+11.9 \pm 0.6$	$13.24^{+1.40(0.13)}_{-1.50(0.16)}$	$+13.0 \pm 3.5$	$40.04^{+4.10(0.04)}_{-4.13(0.05)}$
Si IV	1393.760	$+4.3 \pm 0.2$	$16.30^{+0.78(0.23)}_{-0.87(0.30)}$	$+7.1 \pm 0.6$	$48.57^{+1.64(0.08)}_{-1.67(0.10)}$
Si IV	1402.773	$+4.5 \pm 0.4$	$16.87^{+0.91(0.23)}_{-0.99(0.29)}$	$+6.4 \pm 1.3$	$54.47^{+3.43(0.07)}_{-3.46(0.09)}$

**Table 7.** The ratio of the fluxes in the two-components including the  $1\sigma$  error estimates. The subscripts N and B denote “Narrow” and “Broad” components respectively.

Ion	$\lambda_0$ (Å)	$F_B/F_N$
C IV	1548.204	$0.67 \pm 0.07$
C IV	1550.781	$1.04 \pm 0.15$
N v	1238.821	$0.45 \pm 0.13$
N v	1242.804	$0.43 \pm 0.21$
O VI	1031.912	$0.30 \pm 0.04$
O VI	1037.613	$0.22 \pm 0.05$
Si III	1892.030	$0.66 \pm 0.13$
Si IV	1393.760	$0.75 \pm 0.06$
Si IV	1402.773	$0.61 \pm 0.07$

the broad component having its largest contribution at  $\log T_{\text{form}} \approx 5.1$  with smaller contributions at both lower and higher temperatures ( $\sim 0.2$  for Si IV and O VI and  $\sim 0.4$  for C IV). The ratio of the fluxes in the two components in  $\epsilon$  Eri are given in Table 7. The  $1\sigma$  errors on the flux ratio are somewhat larger than might be expected given the errors in Table 4. This is because of the strong anti-correlation between  $F_B$  and  $F_N$  which has been accounted for in the  $1\sigma$  error estimates given in Table 7. In  $\epsilon$  Eri the flux in broad component is significantly larger, relative to the narrow one, than in the Sun. If the broad and narrow components genuinely represent different physical regions, this suggests that the broad component may increase with stellar activity. This was proposed by Wood et al. (1997) on the basis of a larger sample of stars for which a correlation with the stellar X-ray flux was apparent.

Fig. 13 shows a plot of the ratio of the line fluxes in the two components versus  $\log T_{\text{form}}$ . Although there is a significant difference between the flux ratio deduced from the two C IV lines, the N v and O VI lines do show that the broad component is less important at higher temperatures. In contrast to the results of Peter (2001, his fig. 6), in  $\epsilon$  Eri the Si IV and Si III lines do not show a rapid decrease in the contribution of the broad component at lower temper-

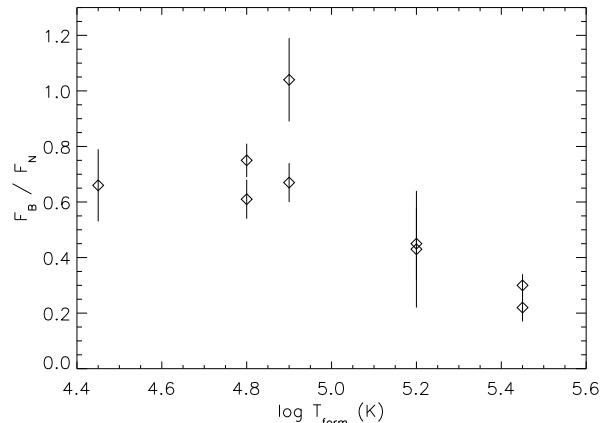


**Figure 13.** Ratio of the flux emitted in the broad component to the that in the narrow component versus  $\log T_{\text{form}}$ .

atures. We point out that the sharp drop in the relative strength of the broad component at low temperatures deduced by Peter (2001) depends on his analysis of the Si II 1533-Å and C II 1335-Å lines (the latter is actually a close blend of two components of the same multiplet). Both of these lines have been excluded from the current study on the grounds that they have significant opacity and hence their profiles can be affected by radiative transfer effects. Also, models of the atmosphere (Sim 2002) suggest that the temperatures of formation adopted by Peter (2001) for these lines are too high, in which case the thermal broadening has been overestimated. The C II 1335-Å line in  $\epsilon$  Eri does show broad wings and the analysis of this line profile will be discussed in later work on chromospheric modelling, including the radiative transfer.

Comparing Fig. 12 and 13 suggests a possible reason for the flattening off of the non-thermal velocities with  $T_e$  above  $10^5$  K when single Gaussian fits are used (see Fig. 1). Above this temperature the contribution of the broad component to the total line flux decreases so that the combined

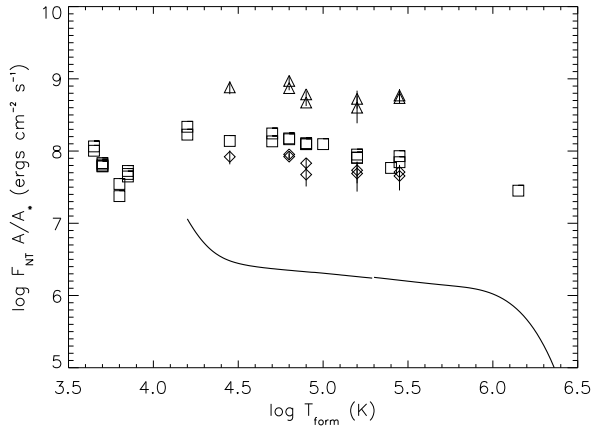


**Figure 14.**  $\log F_{\text{NT}} A/A_*$  versus  $\log T_{\text{form}}$  for 2-component fits (broad components marked with a triangle and narrow components with a diamond). The fluxes are more constant than when a single-Gaussian fit to the line profiles is used. The boxes indicate results using single-Gaussian fits, computed using  $\rho_{\text{ion}}$ . (See Fig. 5 for results using  $\rho$ .) The full line shows the flux required to account for the radiation losses above a given  $T_e$ .

profile becomes dominated by the narrow component. Thus the single-Gaussian fit produces a smaller line width, even though the widths of both the narrow and broad component are not decreasing with  $\log T_{\text{form}}$ . This explanation depends on the Fe XII line flux being dominated by the narrow component, while the mid transition region lines Si III, Si IV, C IV and N V contain significant contributions from both components.

The non-thermal flux in each component for waves travelling at the Alfvén speed, and assuming the same  $P_e$  in both components, is shown in Fig. 14. Only calculations using  $\rho_{\text{ion}}$  are shown since the lines for which two-Gaussian fits have been carried out all form at sufficiently high temperatures that  $\rho_{\text{ion}} \approx \rho$ . The drop in the flux derived for the narrow component (spatially averaged as before) between  $10^5$  K and  $1.4 \times 10^6$  K is now only a factor of 1.8, compared with a factor of 4.5 when single-Gaussian fits are made. The fluxes are still large compared with those required and the wave propagation needs to be investigated. We have no way of telling whether or not the flux in the broad component continues to higher temperatures. If it decreases to the value derived from the Fe XII line, then there are problems in disposing of the energy, unless  $b$  and  $P_e$  are small throughout the broad component region. There would be similar problems regarding deposition of the energy if the broad components were restricted to regions where the magnetic flux does not continue to the corona. As stressed above the broad component flux could continue without being observable in the Fe XII line profile. In this case, the correlation between the degree of the contribution of the broad component to the line profiles and the X-ray flux, found by Wood et al. (1997) is surprising, since the radiative losses should be dominated by the narrow component. It is possible that the X-ray flux and the broad components are related to different aspects of the magnetic field configuration, which themselves have systematic trends. Thus the origin of the broad component

and its relation to coronal heating is still unclear. Energy balance models are required to explore this further.

At lower temperatures, extrapolating the results of Peter (2001) would suggest that the lines are dominated by the narrow component. Certainly, there is no strong evidence for the presence of a second component in the C I or O I intersystem lines. If these lines were dominated by the broad component, the large rise in  $\xi$  (see Fig. 12) when combined with  $\rho_{\text{ion}}$ , would at face value imply an *increase* in the wave flux and an energy source in the low transition region/upper chromosphere. For example, Axford & McKenzie (1992) have suggested that reconnection events involving small flux tubes at the level of the chromosphere or low transition region could generate Alfvén waves. These could be high frequency waves which could propagate to the corona before being damped (McKenzie, Axford & Banaszekiewicz 1995, McKenzie, Banaszekiewicz & Axford 1997). If  $\rho$  is adopted, the wave flux in the chromosphere exceeds that required at higher temperatures (see Section 3) and it is possible that the broadening of the chromospheric lines is the result of a different heating process and not a continuation of either transition region component.

An alternative explanation of the line-widths (of one or both components) is that the ion and electron temperature are not equal and the widths reflect high ion temperatures (see Peter 2001). The idea is attractive given observations of high O VI ion temperatures in polar coronal holes (see Cranmer et al. 1999 and references therein), and proposals by Marsch, Goertz & Richter (1982) and McKenzie et al. (1995, 1997) that damping of Alfvén waves by ion-cyclotron resonance could heat and drive the solar wind. However, to predict the resulting effects on ions in the transition region requires detailed calculations.

## 6 CONCLUSIONS

The excellent properties of the STIS instrument have allowed us to determine the non-thermal motions and line shifts in the outer atmosphere of  $\epsilon$  Eri through analyses of the profiles of optically thin lines. The non-thermal velocity fields are important in semi-empirical modelling of the atmosphere and the results presented here have been used in such models (Sim 2002).

The measured line widths have been used to derive the non-thermal energy content of the atmosphere. The energy which could be carried in acoustic or Alfvén waves has been investigated using the simple WKB approximation. The critical wave periods for this approximation to hold have been expressed in terms of observable parameters, as far as is possible. The unknown parameters are related to the magnetic field. With new models of the outer atmosphere more rigorous calculations could be made of how such waves may or may not propagate to the corona. As concluded from previous studies, the observations appear to rule out acoustic waves as the source of coronal heating.

A detailed analysis of the two-component nature of the mid-transition region lines of Si III, Si IV, C IV, N V and O VI has been carried out, and the results compared with those found for the Sun and other main-sequence stars. It is found that the broad component contributes a larger fraction of the transition region line flux than in the Sun, supporting



the suggestion by Wood et al. (1997) that this component to the flux increases with stellar activity. In agreement with analyses of solar data the broad component is found to be less important in the higher temperature lines of N V and O VI; it might not be significant in the Fe XII line. If so, the correlation between broad transition region lines and stellar X-ray emission found by Wood et al. (1997) is hard to understand, unless both independently reflect systematic changes in the structure and strength of the magnetic fields. In  $\epsilon$  Eri, the broad component is *red-shifted* relative to the narrow component, whereas in the Sun, relative blue shifts are found.

The narrow components are less broad than in the Sun and follow the correlation between  $\xi$  and  $g_*$  found by Wood et al. (1997). We consider that there are fewer difficulties in relating the *narrow* component to the passage of Alfvén waves which could heat the corona, in contrast to Peter's (2001) proposal that this role is played by the broad component.

A large amount of work remains to be done on the theoretical interpretation of the observations. However, the quality of the results from STIS places new constraints on proposed heating mechanisms.

## ACKNOWLEDGMENTS

We wish to thank the referee, P. Ulmschneider, for several useful comments on this manuscript.

SAS acknowledges financial support provided by a PPARC research studentship (PPA/S/S/1999/02862).

## REFERENCES

- Achour H., Brekke P., Kjeldseth Moe O., Maltby P., 1995, ApJ, 453, 945
- Arnaud M., Rothenflug R., 1985, A&AS, 60, 425
- Axford W. I., McKenzie J. F., 1992, in Marsch E., Schwenn R., eds, Solar Wind Seven. Pergamon, Oxford, p. 1
- Ayres T. R., Linsky J. L., Simon T., Jordan C., Brown A., 1983a, ApJ, 274, 784
- Ayres T. R., Stencel R. E., Linsky J. L., Simon T., Jordan C., Brown A., Engvold O., 1983b, ApJ, 274, 801
- Berger R. A., Bruner E. C., Jr., Stevens R. J., 1970, Sol. Phys., 12, 370
- Boland B. C., Engstrom S. F. T., Jones B. B., Wilson R., 1973, A&A, 22, 161
- Boland B. C., Dyer E. P., Firth J. G., Gabriel A. H., Jones B. B., Jordan C., McWhirter R. W. P., Monk P., Turner R. F., 1975, MNRAS, 171, 697
- Blair B. & Andersson B.-G., 2001, The *FUSE* Observer's Guide, Version 3.0
- Brekke P., Hassler D. M., Wilhelm K., 1997, Sol. Phys., 175, 349
- Brown A., Jordan C., Stencel R. E., Linsky J. L., Ayres T. R., 1984, ApJ, 283, 731
- Browning P. K., 1991, Plasma Phys. Control. Fusion, 33, 539
- Bruner E. C., McWhirter R. P. W., 1979, ApJ, 231, 551
- Bruner E. C., Jr., Jones R. A., Rense W. A., Thomas G. E., 1970, ApJ, 162, 28
- Carlsson M., 1986, Uppsala Astronomical Observatory, Report No. 33
- Chae J., Schühle U., Lemaire P., 1998, ApJ, 505, 957
- Cook J. W., Cheng C.-C., Jacobs V. L., Antiochos S. K., 1989, ApJ, 338, 1176
- Cranmer S. R., Field G. B., Kohl J. L., 1999, ApJ, 518, 937
- Cross R., 1988, An Introduction to Alfvén Waves. Adam Hilger, Bristol
- Dere K. P., Mason H. E., 1993, Sol. Phys., 144, 217
- Doschek G. A., Feldman U., VanHoosier M. E., Bartoe J.-D. F., 1976, ApJS, 31, 417
- Doyle J. G., O'Shea E., Erdélyi R., Dere K. P., Socker D. G., Keenan F. P. 1997, Sol. Phys., 173, 243
- Edlén B., 1934, Nova Acta R. Soc. Uppsala IV, 9, 6
- Feldman U., Doschek G. A., VanHoosier M. E., Purcell J. D., 1976, ApJS, 31, 445
- Griesmann U., Kling R., 2000, ApJL, 536, L183
- Hallin R., 1966, Ark. Fys., 31, 511
- Hansteen V. H. 1993, ApJ, 402, 741
- Hollweg J. V., 1991, in Ulmschneider P., Priest E. R., Rosner R., eds, Mechanisms of Chromospheric and Coronal Heating. Springer-Verlag, Berlin, p. 423
- Jordan C., 1991, in Ulmschneider P., Priest E. R., Rosner R., eds, Mechanisms of Chromospheric and Coronal Heating. Springer-Verlag, Berlin, p. 300
- Jordan C., 2000, Plasma Phys. Control. Fusion, 42, 415
- Jordan C., McMurry A. D., Sim S. A., Arulvel M. 2001a, MNRAS, 322, L5
- Jordan C., Sim S. A., McMurry A. D., Arulvel M. 2001b, MNRAS, 326, 303
- Jordan C., Sim S. A., McMurry A. D. 2001c, in Conf. Proc. Cool Stars, Stellar Systems and the Sun. 12th Cambridge Workshop, in press
- Jordan C., Ayres T. R., Brown A., Linsky J. L., Simon T., 1987, MNRAS, 225, 903
- Kelly R. L., 1987, J. Phys. Chem. Ref. Data, 16 (Suppl. 1), 1
- Kjeldseth-Moe O., Nicolas K. R., 1977, ApJ, 211, 579
- Kurucz R. L., Bell B. 1995, Atomic Line Data CD-ROM No. 23, Cambridge, Mass.: S.A.O.
- Landi E., Landini M., Dere K. P., Young P. R., Mason H. E., 1999, A&AS, 135, 339
- Linsky J. L., Ayres T. R., 1978, 220, 619
- Linsky J. L., Wood B. E., 1994, ApJ, 430, 342
- Macpherson K. P., Jordan C., 1999, MNRAS, 308, 510
- Macpherson K. P., Jordan C., Smith G., 1999, in Vial J.-C., Kaldeich-Schümann B., eds, Proc. 8th SOHO Workshop, ESA Special Publications 446, p. 461
- McKenzie J. F., Axford W. I., Banaszekiewicz M., 1997, Geophys. Res. Lett., 24, 2877
- McKenzie J. F., Banaszekiewicz M., Axford W. I., 1995, A&A, 303, L45
- Marsch E., Goertz C. K., Richter K., 1982, J. Geophys. Res., 5, 111
- Meyer F., 1976 in Bonnet R.-M., Delache Ph., eds, The Energy Balance and Hydrodynamics of the Solar Chromosphere and Corona. Nice Observatory, Nice, p. 111
- Montesinos, B., Jordan C., 1993, MNRAS, 264, 900
- Narain, U., Ulmschneider, P., 1990, Space Sci. Rev., 54, 377
- Narain, U., Ulmschneider, P., 1996, Space Sci. Rev., 75, 453
- Osterbrock D. E., 1961, ApJ, 134, 347

- Peter H. 1999, *ApJ*, 516, 490  
 Peter H. 2000a, *A&A*, 360, 761  
 Peter H. 2000b, *A&A*, 364, 933  
 Peter H. 2001, *A&A*, 374, 1108  
 Peter H., Judge P. G. 1999, *ApJ*, 522, 1148  
 Rüedi L., Solanki S. K., Mathys G., Saar S. H. 1997, *A&A*, 318, 429  
 Saar S. H., Osten R. A. 1997, *MNRAS*, 284, 803  
 Sandlin G. D., Bartoe J.-D. F., Brueckner G. E., Tousey R., VanHoosier M. E., 1986, *ApJS*, 61, 801  
 Scharmer G. B. Carlsson M. 1985, *J. Comp. Phys.*, 59, 56  
 Seely J. F., Feldman U., Schühle U., Wilhelm K., Curdt W., Lemaire P., 1997, *ApJL*, 484, L87  
 Sim S. A., 2002, D.Phil. Thesis, University of Oxford  
 Thatcher J. D., Robinson R. D., Rees D. E. 1991, *MNRAS*, 259, 14  
 Vernazza J. E., Avrett E. H., Loeser R. 1981, *ApJS*, 45, 635  
 Wood B. E., Linsky J. L., Ayres T. R. 1997, *ApJ*, 478, 745  
 Zirker J.B. 1993, *Sol. Phys.*, 148, 43

## APPENDIX: BROAD WINGS DUE TO NON-ISOTROPIC VELOCITY FIELDS

The purpose of this appendix is to draw attention to the possibility that the broad wings in observed transition region line profiles (Section 5) might be due to a non-isotropic non-thermal velocity field, rather than being the result of emission in two physically distinct atmospheric components.

In deriving equation (1), it is assumed that the non-thermal velocities are described by a Maxwellian distribution in three-dimensions. There is no direct observational evidence to justify this assumption and it is interesting to examine the consequences of it being incorrect.

Suppose that the non-thermal motions are the result of oscillations caused by transverse waves propagating along magnetic field lines. Consider a small volume element of material which is threaded by magnetic field lines which are at an angle  $\theta$  to the observers line-of-sight. The non-thermal motions will be restricted to the plane perpendicular to the magnetic field. Assuming, for simplicity, that the non-thermal motions within this plane are described by a 2-D Maxwell distribution, the observed profile of an emission line emitted by the material in the volume element will be

$$I(\lambda) = \frac{C}{\sqrt{b^2 + a^2 \sin^2 \theta}} \exp(-\lambda^2 / (b^2 + a^2 \sin^2 \theta)) \quad (\text{A1})$$

where  $\lambda$  is the wavelength measured relative to line centre,  $I(\lambda)$  is the intensity at wavelength  $\lambda$  and  $C$  is a constant.  $a$  and  $b$  specify the widths of the 2-D Maxwell distribution of non-thermal velocities and the 3-D Maxwell distribution of thermal velocities respectively. Line broadening from sources other than thermal and non-thermal motions have been neglected.

In order to obtain the profile that would be observed from the entire star it is necessary to assume a distribution for the angle  $\theta$ . Here we adopt the simplest assumption, that the distribution is spherically symmetric. This would be a reasonable assumption for a star if the magnetic field were completely disordered (randomly oriented) on macroscopic scales. It would also be approximately valid if the field

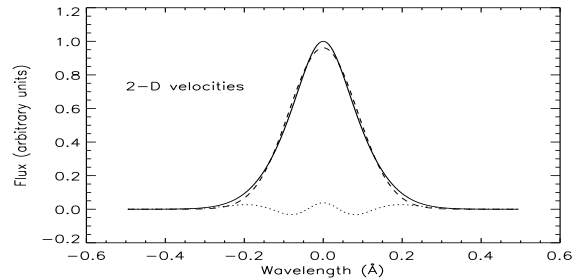


**Figure A1.** Profile computed from Equation (A2) (solid line) with Gaussian over-plotted (broken line) and residual (dotted line). The values  $a = 0.15 \text{ \AA}$  and  $b = 0.05 \text{ \AA}$  have been adopted.

was purely radial over an (unresolved) hemispherical stellar surface: the calculations presented here are appropriate for emission from a hemisphere but they do not account for the excess emission off the limb from material in the back hemisphere of the star. If emission from the back hemisphere were included in the calculation it would enhance the strength of the broad wings predicted in the 2-D case. The spherically symmetric distribution will also be appropriate for spatially resolved observations of the Sun, provided that the field is tangled on scales less than the spatial resolution or contains both radial and closed loop field configurations. If the field were locally ordered, then it would be necessary to adopt a more complex distribution. Adding up different  $\theta$  angle strips from centre to limb, the total stellar profile in the presence of 2-D non-thermal motions is

$$I(\lambda)_{2\text{-D}} \propto \int_0^{\pi/2} \frac{\sin \theta d\theta}{\sqrt{b^2 + a^2 \sin^2 \theta}} \exp(-\lambda^2 / (b^2 + a^2 \sin^2 \theta)) . \quad (\text{A2})$$

Alternatively, consider the case of non-thermal motions generated by longitudinal waves propagating along the magnetic field. The non-thermal velocities are then confined to only one dimension, along the field. By analogy with the case given above the total stellar profile is

$$I(\lambda)_{1\text{-D}} \propto \int_0^{\pi/2} \frac{\sin \theta d\theta}{\sqrt{b^2 + a^2 \cos^2 \theta}} \exp(-\lambda^2 / (b^2 + a^2 \cos^2 \theta)) . \quad (\text{A3})$$

Figs. A1 and A2 shows profiles calculated from equations (A2) and (A3), respectively. In both cases the thermal width has been chosen to be appropriate to the C IV lines,  $b = 0.05 \text{ \AA}$ . The non-thermal width parameter ( $a$ ) was chosen arbitrarily (see below). In each figure a single-Gaussian fit to the line and the residual for that fit are plotted. These should be compared with the fits and residuals for the observed profiles shown in Fig. 11. Two-Gaussian fits have been performed on the profiles calculated from equations (A2) and (A3). The results of these fits (fluxes and widths for the two components) are given in Table A1.

The values of  $a$  used in the calculations were chosen so that the width of the narrow Gaussian fit component is comparable to that observed for C IV. For the 2-D case  $a = 0.15 \text{ \AA}$  and for the 1-D case  $a = 0.32 \text{ \AA}$ .

Figs. A1 and A2 show that these non-isotropic velocity distributions produce line profiles that have broader wings

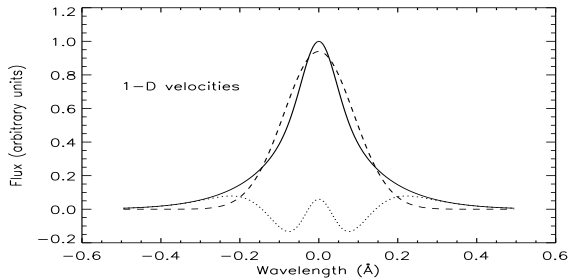


**Figure A2.** Profile computed from Equation (A3) (solid line) with Gaussian over-plotted (broken line) and residual (dotted line). The values  $a = 0.32 \text{ \AA}$  and  $b = 0.05 \text{ \AA}$  have been adopted.

**Table A1.** Two-Gaussian fit to the computed profiles for a 2-D non-thermal velocity distribution (equation A2) and a 1-D non-thermal velocity distribution (equation A3). The fluxes ( $F$ ) are given in arbitrary units and line widths ( $\Delta\lambda$ , FWHM) are given in  $\text{\AA}$ . The subscripts  $N$  and  $B$  refer to the narrow and broad Gaussian components.

	$F_N$	$\Delta\lambda_N$	$F_B$	$\Delta\lambda_B$
2-D case	0.0571	0.137	0.1560	0.244
1-D case	0.0933	0.132	0.1253	0.394

than a Gaussian, in qualitative agreement with the observed profiles. The broad wings are relatively stronger in the 1-D than 2-D case. The width of the broad Gaussian component fitted to the calculated profile is in very good agreement with that fitted to the observed C IV profiles for the 1-D case, but is too narrow in the 2-D case. There is some quantitative disagreement between these calculations and the observations. In both cases, the flux ratio of the broad to narrow component is too large, compared with the observations. The 1-D flux ratio is consistent with the observed 1550- $\text{\AA}$  flux ratio at the 2- $\sigma$  level, but is very different from the 1548- $\text{\AA}$  ratio. Also, the computed profiles are symmetric about line centre while the observed broad components are all redshifted relative to the narrow components by several  $\text{km s}^{-1}$ . In the model used here (which neglects the line formation process), to produce a redshifted broad component would require a mean net flow away from the observer. To shift the broad component relative to the narrow for the 1-D case would require a redshift that is largest in the regions with small  $\theta$ , while for the 2-D case the redshift would need to be largest in regions with large  $\theta$ .

In conclusion, it is apparent from Figs. A1 and A2 that a non-isotropic velocity distribution could predict line profiles with broad wings without the need to invoke a physically distinct second component to the emission. Although the discussion here has used the passage of transverse and longitudinal waves as examples, it is noted that the results are general to any situation where the non-thermal velocities are confined to only one or two-dimensions, whatever their origin. It is not proposed that the extremely simple one and two-dimensional non-thermal velocity distributions used here are realistic; we wish only to draw attention to the fact that such distributions can naturally lead to non-

Gaussian profiles whose properties are similar to those of observed transition region lines.